

Article

# Properties of Nitrogen/Silicon Doped Vertically Oriented Graphene Produced by ICP CVD Roll-to-Roll Technology

Petr Rozel <sup>1</sup>, Darya Radziuk <sup>2,\*</sup>, Lubov Mikhnavecs <sup>2</sup>, Evgenij Khokhlov <sup>1</sup>, Vladimir Shiripov <sup>1</sup>, Iva Matolínová <sup>3</sup> , Vladimír Matolín <sup>3</sup>, Alexander Basaev <sup>4</sup>, Nikolay Kargin <sup>5</sup> and Vladimir Labunov <sup>2</sup>

<sup>1</sup> IZOVAC Technologies Ltd., M. Bogdanovicha Str. 155-907, 220040 Minsk, Belarus; rozel@izovac.com (P.R.); e-khokhlov@izovac.com (E.K.); dr\_shiripov@izovac.com (V.S.)

<sup>2</sup> Belarusian State University of Informatics and Radioelectronics, P. Brovki Str. 6, 220013 Minsk, Belarus; happy.bazinga@gmail.com (L.M.); labunov@bsuir.by (V.L.)

<sup>3</sup> Faculty of Mathematics and Physics, Charles University, V Holešovičkách 2, 18000 Prague 8, Czech Republic; imatol@mbox.troja.mff.cuni.cz (I.M.); matolin@mbox.troja.mff.cuni.cz (V.M.)

<sup>4</sup> SMC (Technological Centre), Square Shokin 1, 124498 Zelenograd (Moscow), Russian; a.basaev@tcen.ru

<sup>5</sup> National Research Nuclear University “MEPhi”, Kashirskoe shosse 31, 115409 Moscow, Russian; krgn@ya.ru

\* Correspondence: radziuk@bsuir.by; Tel.: +375-17-293-8803

Received: 5 December 2018; Accepted: 14 January 2019; Published: 19 January 2019



**Abstract:** Simultaneous mass production of high quality vertically oriented graphene nanostructures and doping them by using an inductively coupled plasma chemical vapor deposition (ICP CVD) is a technological problem because little is understood about their growth mechanism over enlarged surfaces. We introduce a new method that combines the ICP CVD with roll-to-roll technology to enable the in-situ preparation of vertically oriented graphene by using propane as a precursor gas and nitrogen or silicon as dopants. This new technology enables preparation of vertically oriented graphene with distinct morphology and composition on a moving copper foil substrate at a lower cost. The technological parameters such as deposition time (1–30 min), gas partial pressure, composition of the gas mixture (propane, argon, nitrogen or silane), heating treatment (1–60 min) and temperature (350–500 °C) were varied to reveal the nanostructure growth, the evolution of its morphology and heteroatom’s intercalation by nitrogen or silicon. Unique nanostructures were examined by FE-SEM microscopy, Raman spectroscopy and energy dispersive X-Ray scattering techniques. The undoped and nitrogen- or silicon-doped nanostructures can be prepared with the full area coverage of the copper substrate on industrially manufactured surface defects. Longer deposition time (30 min, 450 °C) causes carbon amorphization and an increased fraction of sp<sup>3</sup>-hybridized carbon, leading to enlargement of vertically oriented carbonaceous nanostructures and growth of pillars.

**Keywords:** vertically oriented graphene (VOG); inductively coupled plasma chemical vapor deposition (ICP CVD); roll-to-roll technology; supercapacitor; Li-ion battery

## 1. Introduction

The importance of spatial alignment of one-dimensional carbonaceous nanomaterials (nanotubes, nanowires, nanorods) to their applications such as field emitters, electromechanical actuators, gas sensors, and catalysts has been well recognized [1–6]. These spatial alignment effects have been further extended to two-dimensional (2D) nanostructures, such as graphene. 2D graphene has attracted attention due to its high surface-area-to-volume ratio and extraordinary electrical properties on atomically thin sheets because of a tiny overlap between valence and conductance bands [7]. Another

advantage of graphene is due to its free-standing atomic crystals structure presenting molecular planes unprotected from the immediate environment which are stable under ambient conditions, and exhibit high crystal quality, continuously spread on a microscopic scale [8].

Vertically oriented graphene (VOG) have attracted interest because of their unique orientation, exposed sharp edges and non-stacking morphology that can be integrated into many functional devices including supercapacitors [9], Li-ion batteries [10], biosensors [11] and catalysts [12]. Superior chemical stability, higher electron conductivity and ion diffusivity, the cycling stability and larger surface area of VOG make it a competitive material for specific capacitance and its retention [13]. In Li-ion battery application, additional sites in VOG such as cavities, edges of the graphene basal planes, and those with hydrogen terminated groups act as hosts for charge carriers, thereby effectively increasing capacity compared to natural graphite or activated carbon [14,15]. The storage capacity, Li atom diffusion and catalytic property of VOG can be significantly enhanced via intercalation with various materials (e.g., N, Si, MnO<sub>2</sub>, etc.) [16–22]. The higher electrical conductivity of VOG is related to the presence of pores and can be obtained if nitrogen acts as a dopant near the edge of the density of states in the sp<sup>3</sup>-hybridized carbon matrix, thereby promoting the 2D curvature and attachment to the sp<sup>2</sup>-hybridized carbon clusters [23]. The thinner edge planes of VOG lead to a higher specific capacitance arising from much larger area-specific edge topology than basal surface planes. Higher sp<sup>2</sup> hybridization content improves the charge storage capability, and the sp<sup>3</sup>-hybridized carbon increases the charge transfer resistance. However, for enhanced VOG performance in a specific surface area, its composition and the interlayer spacing should be well controlled during the preparation process.

Among the many methods used for VOG preparation, chemical vapor deposition (CVD) has demonstrated great potential for economical mass production, however, it requires elevated temperatures (800–1000 °C) and the costs for industrial manufacturing are high [24–26]. VOG growth can be achieved at lower temperatures (<800 °C) if the inductively coupled plasma chemical vapor deposition method (ICP CVD) is used, and it has become a key technique for the synthesis of high-quality coating without material damage and undesired defect formation [27–29]. Another advantage of CVD is due to the broad choice of available substrates for VOG preparation (e.g., SiO<sub>2</sub> and Al<sub>2</sub>O<sub>3</sub> [30], Si [31], Ni [32], stainless steel [33–36], Cu [37–40], Co [41], Al and TiO<sub>2</sub> [42], Al<sub>2</sub>O<sub>3</sub> [43], and Pt [44–46]). However, the VOG growth by ICP CVD is a complex, not well understood process because the changes in the VOG structure depend on a plasma source and a series of technological parameters including the type of a precursor gas (e.g., CH<sub>x</sub> ( $x = 1-3$ ), CF<sub>4</sub>, CHF<sub>3</sub>, or C<sub>2</sub>F<sub>6</sub>), gas composition and its partial pressure, the deposition time, and heating treatment [47].

Extensive research has been performed to reveal the basics of the VOG growth mechanism and development of its morphology, especially during the initial nucleation period [48]. VOG can develop a wave shape by using a CH<sub>4</sub>/H<sub>2</sub> gas mixture, with a smaller interlayer spacing and greater thickness, if only CH<sub>4</sub> is used. However, there is a limitation in the use of methane in the ICP CVD method that is associated with the number of defects in the VOG. The growth rate of VOG can be increased by using C<sub>2</sub>H<sub>2</sub>, providing reactive C<sub>2</sub> carbon dimers that play important role in the evolution of critical nuclei into vertically oriented carbonaceous nanostructures. Other reactive species include free radicals, ions and plasma reaction products [49]. Propane could be a useful precursor gas as its pyrolysis reaction products are 1-C<sub>3</sub>H<sub>7</sub>, 2-C<sub>3</sub>H<sub>7</sub>, C<sub>3</sub>H<sub>6</sub>, which rapidly decompose into C<sub>2</sub> species, e.g., C<sub>2</sub>H<sub>4</sub> and C<sub>2</sub>H<sub>2</sub> [50–52]. The presence of Ar can enhance the formation of critical species that are used for the VOG growth, i.e., C<sub>2</sub>, H and ionic clusters of carbon, thereby significantly improving the plasma stability, resulting in a VOG network or VOG consisting of intercepted diamond carbons. Ionic clusters of carbon C<sub>n</sub>H<sub>x</sub> ( $n \geq 2$ ,  $x = 1, 2, 3$ ), Ar and H<sub>2</sub> ions/molecules, and energetic electrons serve as the building species for VOG growth via the ionic chain polymerization process. Accurate control over the gas proportion can determine the type of carbon hybridization (sp<sup>1</sup>, sp<sup>2</sup> or sp<sup>3</sup>) and crystallinity (amorphous  $\alpha$ -C, mono- or polycrystalline carbon), thereby strongly influencing the VOG morphology and structure. However, it is difficult to define a certain precursor gas ratio for all the ICP

CVD systems, even of the same type, due to the difference in plasma characteristics and operating conditions [27].

The formation of high quality VOG requires effective removal of amorphous  $\alpha$ -C carbon; this can be performed by introducing etchants such as atomic hydrogen or oxygen, excited nitrogen and hydroxyl radicals (OH radical) [53]. However, care should be taken over the proper choice of effective etchants in order not to destroy  $sp^2$ - and  $sp^3$ -hybridized carbon in the VOG nanostructure. Among such effective etchants, nitrogen can promote the dissociation of  $CH_4$ , that is, to lose H atoms and to form  $C_2$  and CN species, both of which were observed in  $N_2$ -containing ICP CVD systems during VOG growth [54,55].  $N_2$  can also change the VOG morphology and structure during its growth by substituting C atoms and introducing additional defects. As a result, nitrogen-doped VOG appear with reduced alignment and highly branching morphology, and with no obvious difference in the height and interlayer spacing [56].

Oxygen can control the synthesis of graphene by influencing the carbon network during the growth via the charge transfer process between the oxygen and Cu atoms to the carbon atom at the O-rich Cu sites [57]. The hydrogen prevents the formation of surface oxides on the metallic substrate. During the reaction, the hydrogen terminated substrate surface allows wrinkle-free graphene growth without any grain boundary [58]. The electronic properties of VOG can be controlled by introducing various heteroatoms (i.e., dopants) into VOG such as N, B, S, Al, Au, Ag, Fe, P, Sn and Si in order to increase the catalytic activity, long-term operational stability, surface reactivity and thermal conductivity [59–61]. Among the heteroatoms used as dopants, Si can modulate the electronic structure of graphene by opening a band gap, and enhance the charge carrier mobility that becomes comparable to that of boron-doped graphene [62,63]. The as-synthesized silicon-doped graphene film shows a considerably high carrier mobility of about  $660 \text{ cm}^2/\text{V}\cdot\text{s}$  at room temperature. Besides, silicon-doped graphene demonstrates great potential for storing hydrogen and enhanced adsorption of different molecules [64]. Doping of graphene by silicon is still rare and represents an emerging field, especially in catalytic research [65]. However, it is difficult to dope silicon atoms into a graphene lattice with stable Si-C bonds, because the atomic radius of silicon atoms (117 pm) is much larger than that of carbon atoms (77 pm). This limits the fundamental knowledge and understanding of the silicon doping mechanism of graphene [17].

Another important parameter in ICP CVD is the pressure that influences the plasma energy, formation of active species and VOG growth process, which is not simply proportional to the pressure or gas flow rate because of the complex plasma chemistry process [66]. In addition, the higher substrate temperature enhances the surface reaction kinetics by increasing the nucleation sites on both the substrate and the as-grown VOG layers [67]. Until now the accelerated growth of VOG coating on an enlarged surface area remains a critical prerequisite for industrial applications because of the low yield of the final product. For practical applications, lower temperature during the ICP CVD process will allow the use of flexible substrates (e.g., plastics), thereby opening new applications of VOG in the area of flexible electronic devices. Therefore, there is a need for a new technology that allows the up-scaling of VOG growth at a lower cost.

Coupling ICP CVD with roll-to-roll technology (RtR) will enable VOG growth and its mass production as a continuous film over enlarged surfaces [68]. The RtR method supports regular VOG formation on a larger scale, because the processability is good and its scalability is high, thereby making it suitable for mass production. However, combining these two methods requires extensive research effort in order to understand the VOG growth mechanism and reveal the influential parameters that control the morphology, crystallinity and composition during the formation and doping processes of vertically oriented carbonaceous nanostructures. The questions to be answered are: (1) Why does VOG prepared from various precursor gases, exhibit different adhesion to the substrate and develop individual topologies? (2) What are the influential technological parameters for preferential VOG growth, the increased thickness of VOG coating and a defined number of graphene layers in it? (3) How can one control the porosity and crystallinity of VOG coating and its efficient doping by different

compounds to meet industrial needs for the mass production of advanced functional electronic devices? At present, there is no general agreement on a unified theory to predict the VOG growth mechanism. New pathways for the desired VOG morphology and its coating thickness will be discovered by using specific technological parameters (i.e., plasma temperature, gas composition and flow rate, time of deposition and heating treatment).

Here, for the first time, we report a new method, which is based on the coupling of the ICP CVD system with RtR technology and was applied for in situ VOG formation and doping on a moving copper foil substrate. In this work, we demonstrated that the VOG coating is simultaneously produced and doped by nitrogen or silicon in the presence of propane as a precursor gas. As a novelty, we examined the dependence of a set of technological parameters of this unique technology on the VOG crystalline structure and morphology during the growth and doping processes. In particular, we provide new facts about the coexistence of VOG growth and heteroatom doping, which was enabled at a reduced substrate temperature in the range from 350 to 500 °C; the effects of deposition time (1–30 min) and heating treatment (<60 min) were also considered.

## 2. Materials and Methods

### 2.1. Materials

Propane (C<sub>3</sub>H<sub>8</sub>, 99.6%) was purchased from Linde gas. Argon (Ar, 99.9%), nitrogen (N<sub>2</sub>, 99.9%) and silane (SiH<sub>4</sub>, 99.9%) were obtained from EuroGroup (Minsk, Belarus). A copper foil (99.8%, 35 μm thickness, HTE-Cu for Li-ion batteries application) was purchased from Ostec GmbH (Klipphausen, Germany).

### 2.2. Methods

An inductively coupled plasma chemical vapor deposition (ICP CVD) system consisting of a vacuum chamber with a 22 cm diameter radio frequency (RF) inductive coil connected to a matching block (MB) was designed by IZOVAC Technologies Ltd. (Minsk, Belarus). This system was employed to prepare vertically oriented graphene on a moving copper foil substrate as illustrated in Figure A1 (Appendix A). This ICP CVD system was coupled with the roll-to-roll apparatus, aiming at mass production of high-quality electrodes based on VOG grown on the copper foil through the rolling over process from one roll to the other (Figure 1A). Technological devices, which are placed between these rolls, form a VOG coating on the moving copper foil surface during the rolling over process. By request, these technological devices can be placed on the inner and outer sides of the copper foil surface in order to produce VOG nanostructures from both sides of the substrate. The copper foil substrate was heated to an elevated temperature in a range up to 500 °C by a heater and this temperature was kept for 20–60 min during the plasma process. A heater placed inside a holder drum was used to control the temperature of the copper foil via a K-type thermocouple stuck on the sample surface. VOG coating was produced in a working atmosphere consisting of {C<sub>3</sub>H<sub>8</sub> + Ar}, {C<sub>3</sub>H<sub>8</sub> + Ar + N<sub>2</sub>} or {C<sub>3</sub>H<sub>8</sub> + Ar + SiH<sub>4</sub>} gas mixtures by varying the propane/argon partial pressure ratio as 1/10, 2/5 and 4/5 assuming the maximal volume of Ar ~500 cm<sup>3</sup> (std. dev. ± 1%). Different VOG nanostructures were prepared via various technological parameters such as deposition time (min), heating time (min) and temperature (°C), see more details in Table 1.

In particular, the deposition time varied from 1 to 30 min, the C<sub>3</sub>H<sub>8</sub> flow rate used was from 50 to 400 sccm and the total pressure was in the range from 0.8 to 1.4 Pa for the preparation of undoped VOG; 1.0 and 1.5 Pa were used for the production of two types of nitrogen-doped VOG and 1.5 Pa was used for the doping of VOG by silicon. A heater was employed to thermally treat a sample inside a holder drum at 350, 450 or 500 °C.

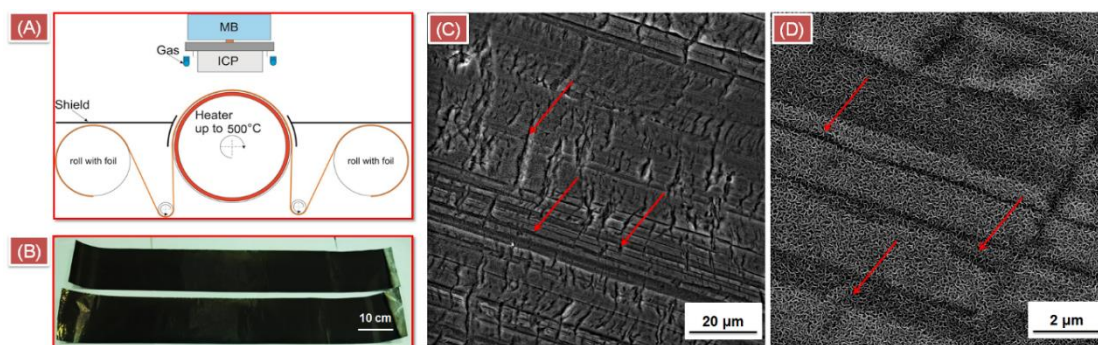


**Figure 1.** (A) Schematic illustration of the ICP CVD roll-to-roll apparatus for the mass production of VOG coating on a moving copper foil substrate. This technology enables preparation of an electrode with a VOG grown at lower processing temperature by using a radio frequency (RF) generator and a matching block (MB) as a plasma source; (B) True color photo images of the VOG-coated copper foil being prepared by using this technology (deposition time: 10 min, heating time/temperature: 40 min/450 °C, total pressure of {C<sub>3</sub>H<sub>8</sub> + Ar} gas mixture: 1 Pa; (C,D) representative FE-SEM images of this VOG coating. Red arrows show surface defects of the copper foil, which occurred after industrial manufacturing.

**Table 1.** Technological parameters of the ICP CVD roll-to-roll technology for the preparation of vertically oriented graphene nanostructures in various gas mixtures.

Sample	Deposition Time, min	Heating Time (min)/T (°C)	Pressure (+Ar), Pa	C <sub>3</sub> H <sub>8</sub> , sccm	N <sub>2</sub> , Pa	SiH <sub>4</sub> , sccm
1	1	40/450	1	200	–	–
2	5	40/450	1	200	–	–
3	10	40/450	1	200	–	–
4	15	40/450	1	200	–	–
5	30	40/450	1	200	–	–
6	5	40/450	0.8	50	–	–
7	10	20/350	1	200	–	–
8	10	60/500	1	200	–	–
9	10	40/450	1.4	400	–	–
N1	10	45/450	1	200	0.5	–
N2	10	45/450	1.5	200	1	–
S1	10	45/450	1.5	200	–	50
S2	10	45/450	1.5	200	–	100

sccm: standard cubic centimeter per minute.

### 2.3. Characterization

The synthesized VOG substrates were characterized through several methods: field emission scanning electron microscopy (FE-SEM), energy dispersive X-ray spectroscopy (EDX) and confocal Raman microscopy. The morphology of prepared VOG materials was analyzed by FE-SEM using a MIRA III (Tescan Brno, Brno, Czech Republic) at primary electron energy of 30 keV. The bulk elemental composition of prepared VOG coatings was obtained by using a SEM S-4800 microscope equipped with an EDX spectrometer at electron energy of 20 keV (Hitachi, Tokyo, Japan).

Raman spectra were recorded by using a 3D inverted confocal Raman microscope Confotec NR500 from SOL Instruments Ltd. (Belarusian-Japanese joint venture “SOLAR TII”, Minsk, Belarus). The Si wafer with the characteristic Raman line at 520 cm<sup>-1</sup> was taken as a reference for calibration, baseline and background correction during the integration time from 0.3 to 1 s. A linearly polarized diode laser beam at 473 nm excitation wavelength was focused through the objectives with the 100× magnification for Raman spectra acquisition with a grating of 600 gr/mm blazed at 600 nm under ambient air. The laser power was attenuated by using neutral density filters, which allow the transmission of a laser beam with respect to the optical density of the filter according to the equation  $OD = -\log(T)$  with

$T = I/I_0$  ( $I$ —transmitted intensity and  $I_0$ —incident laser intensity). The following values of OD ( $T$ ) were used 0.6 (25), 0.3 (50) and no filter (100).

Each sample was analyzed by calculating the crystallite size of carbonaceous nanostructures ( $L_a$ , Å) using the following equation [69]:

$$L_a = \frac{(2.4 \times 10^{-10})\lambda_{laser}^4}{IntD/IntG} \quad (1)$$

$\lambda_{laser}$  is the laser excitation wavelength (473 nm) and IntD/IntG is the ratio of intensities (peak heights) of D and G bands (designated as “R”).

### 3. Results and Discussion

The unique ICP CVD roll-to-roll technology (Figure 1A) allows the formation of a uniform vertically oriented graphene (VOG) coating being continuous across surface steps and boundary grains of the copper foil with the full area coverage at the centimeter scale (Figure 1B). FE-SEM proves the formation of a uniform 2D coating at the microscale (Figure 1C,D), which is also prepared on the surface defects of the copper foil caused during the industrial manufacturing process. The carbonaceous coating consists of individual 2D VOG (Figure A2).

VOG can be considered as networks of carbonaceous nanostructures, which are vertically oriented on the substrate surface. As graphene (i.e., an allotrope form of carbon consisting of a single layer of carbon atoms arranged in a hexagonal lattice) has a van der Waals diameter of carbon of about 0.345 nm [7]. In this work, we also examined the effects of the following technological parameters on the morphology (i.e., shape, height) and content of VOG coatings: (1) deposition time at isothermal (450 °C) and isobaric (1.0 Pa) conditions; (2) partial pressure of propane by varying heating time and temperature; (3) partial pressure of nitrogen at isothermal (450 °C) conditions, and (4) partial pressure of silane at isothermal (450 °C) conditions.

#### 3.1. Effect of Deposition Time at Isothermal (450 °C) and Isobaric (1.0 Pa) Conditions

We investigated the evolution of the VOG morphology as a function of deposition time under isothermal (450 °C) and isobaric (1.0 Pa) conditions of synthesis (Samples 1–5 in Table 1).

FE-SEM micrographs show that longer deposition time leads to an enlargement in VOG leaves, which develop a less curved surface and the amount of coating increasing from ~203 nm (deposition time: 5 min, Figure 2A), 373 nm (10 min, Figure 2B) to 508 nm (15 min, Figure 2C), see Table 2. Most VOG coatings are supported by carbonaceous nanostructures that grow in the direction parallel to the Cu substrate as indicated by red arrows. However, after 30 min of deposition, vertically oriented pillars appeared with a mean diameter of ~36 nm, developing on top of the VOG edges (Figure 2D). The average height of this VOG coating was ~570 nm (Table 2).

FE-SEM revealed the presence of a bottom buffer layer in each type of these VOG coatings (Figure A3). The height of the buffer VOG layer increased with longer deposition time: ~34 nm after 5 min, ~43 nm after 10 min, ~65 nm after 15 min, and ~77 nm after 30 min (Table 2 and Figure A3E). It was observed that the buffer layer can be composed of amorphous graphite phase, the formation of which may be attributed to the insufficient time and temperature for the crystallization of carbon during the ICP CVD process [9]. We noticed that the buffer layer growth in a VOG film was self-limited on the copper foil substrate. For a deposition time less than 5 min, the copper surface was fully covered by a thin VOG coating (Figure A4). This full coverage may be explained by the thickening of VOG layers as a result of excess of carbon precipitation provided by propane as a source of carbon [70]. The growth of VOG nanostructures may be considered a step-flow process on the basis of nucleation at the bottom [71]. In this model, two adjacent graphene layers may be connected to each other and form a sealed tapered edge in the form of a zigzag or armchair, yielding thicker carbonaceous pillars (Figure 2D). The closed edges of these pillars may suppress the interlayer shear resulting in a bending rigidity comparable to carbon nanotubes [72].

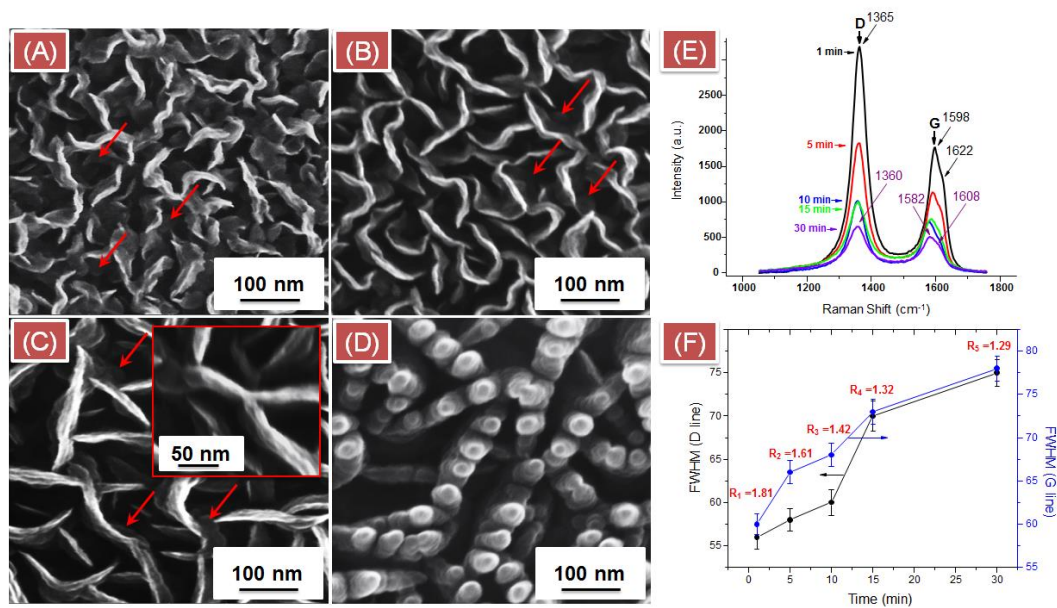


**Figure 2.** (A–D) Representative FE-SEM images of a VOG coating prepared by the ICP CVD roll-to-roll technology after 5, 10, 15 min (inset: a magnified FE-SEM image) and 30 min of deposition time at 450 °C and 1.0 Pa of total pressure; (E) Averaged Raman spectra of a VOG coating acquired at 473 nm excitation wavelength by using a 100× objective and 10 s of integration time. Color coding represents Raman spectra of VOG coatings being formed at different deposition time: 1 min (black, Sample 1), 5 min (red, Sample 2), 10 min (blue, Sample 3), 15 min (green, Sample 4) and 30 min (violet, Sample 5). (F) Full width at half maximum (FWHM) values of the D and G band lines calculated from the averaged Raman spectra versus deposition time. The “R” (in red color) represents the calculated IntD/IntG (peak height) ratio.

**Table 2.** Calculated values of the coating height and the height of the buffer layer derived from the FE-SEM images of VOG nanostructures.

Sample	Height of Coating, nm	Height of Buffer Layer, nm
1	44 ± 3	N/A
2	203 ± 4	34 ± 2
3	373 ± 22	43 ± 2
4	508 ± 29	65 ± 2
5	570 ± 36	77 ± 6
6	189 ± 3	42 ± 3
7	318 ± 5	22 ± 2
8	308 ± 7	63 ± 5
9	489 ± 6	N/A
N1	489 ± 6	N/A
N2	528 ± 8	N/A
S1	497 ± 22	N/A
S2	564 ± 3	N/A

Next, we performed Raman analysis of a VOG coating in order to find out more about the defect density [73], disorder [74] and the carbon amorphization [75] through the characterization of the most prominent D, G, G', {D+G} and 2D' bands (Figures 2E and A5). The presence of all these Raman modes in each spectrum of VOG coating demonstrates the imperfect graphite and disordered carbons [76]. In general, the characteristic peak of D band is located at ~1350 cm<sup>-1</sup> and arises due to a disorder-induced phonon mode, indicating the presence of disorders in the VOG nanostructure [74]. In our VOG coating, the D line appeared at higher wavenumber (e.g., ~1365 cm<sup>-1</sup> after 1 min and ~1360 cm<sup>-1</sup> after 30 min of deposition time), demonstrating the defective nanocrystalline graphite

with a structural disorder (Figure 2E). The characteristic peak of G band is located at  $\sim 1581\text{ cm}^{-1}$  and arises as the stretch vibration mode, indicating the presence of crystalline hexagonal graphite (i.e.,  $\text{sp}^2$ -hybridized carbon network) [75]. In our VOG coating the G band appeared at higher wavenumber ( $\sim 1598\text{ cm}^{-1}$ ) after 1 min, but shifted to a lower frequency  $\sim 1582\text{ cm}^{-1}$  (after 30 min of deposition time) closer to its characteristic value. The peak shift of the G band to a lower frequency by  $\sim 17\text{ cm}^{-1}$  is indicative of the presence of nanocrystalline graphite [75]. 30 min of deposition time leads to a larger shift of the D band (by  $\sim 10\text{ cm}^{-1}$ ) and of the G band, indicating the formation of the amorphous carbon phase, i.e.,  $\text{sp}^2$ -bonded  $\alpha\text{-C}$ , consisting of distorted sixfold rings or rings of other orders involving the  $\text{sp}^3$ -hybridized structure [75]. The G band with a shoulder located at  $\sim 1622\text{ cm}^{-1}$  can be attributed to the D' band with its characteristic peak at  $1620\text{ cm}^{-1}$ , indicating structural disorder and the presence of small grains [73]. The G mode with a D' band as a shoulder is illustrative of the main structural transformation from a monocrystalline to a polycrystalline material [74].

Overall the presence of a triple Raman band vibration, i.e., G', {D+G} and 2D' modes, indicates the layered graphite structure at the nanoscale [74]. In general, the G' band is the second order of the D peak, which is a single peak in a monolayer graphene, i.e., this band is indicative for the stacking order of graphene sheets along the c axis [74], which is in agreement with the decreased intensity of the G' band (Figure A5A). The {D+G} band can arise due to the combination of phonons with different momenta, and indicates nanocrystalline disordered clusters, in agreement with our observation of the D band. In this triple band the 2D' peak is a second order of the D' band, and usually appears in defective samples.

Next, we analyzed the full width at half maximum (FWHM) values and the D/G peak intensity ratio (i.e.,  $\text{IntD}/\text{IntG}$ ) by calculating the peak height of two most prominent D and G Raman modes (Figure 2F). Thirty min of deposition time caused the nonlinear decrease of the  $\text{IntD}/\text{IntG}$  ratio (designated as "R" in Figure 2F), demonstrating the increased fraction of amorphous carbon [75] and ordering of the graphitic structure. Higher D peak and suppression of G' band may indicate the co-existence of the structures with  $\text{sp}^2$  and  $\text{sp}^3$  hybridization during longer deposition time (Figure A5B). Overall the decrease in the  $\text{IntD}/\text{IntG}$  ratio is illustrative of the terminated VOG growth [76]. The FWHM value of both the D and G Raman bands increased after 30 min of deposition time. At this condition an increased broadening of the G band, which is accompanied by the shift of the D' band (by  $\sim 12\text{ cm}^{-1}$ ), and decreased  $\text{IntD}/\text{IntG}$  ratio are indicative of the presence of  $\text{sp}^2$ -hybridized carbon dimers in an ion-implanted diamond structure with  $\text{sp}^3$  hybridization content [75]. This is due to the change in the  $\text{sp}^2$ -hybridized carbon configuration from rings to olefinic groups with their vibrational frequencies lying above the band limit of graphite. We assumed that the carbon dimer density was low because of the presence of amorphous carbon fraction. Carbon amorphization can be derived from the broadening and decrease in intensity of all second order peaks modulated by the G', {D+G} and 2D' bands (Figure A5B). Overall, 30 min of deposition time caused carbon amorphization with increasing  $\text{sp}^3$ -hybridized carbon content in VOG.

### 3.2. Effect of Partial Pressure of Propane

Next, we examined the evolution of the VOG morphology as a function of the partial pressure of propane at isothermal conditions ( $450\text{ }^\circ\text{C}$ ) (Samples 6 and 9 in Table 1) (Figure 3A,D).

Sample 6 represents  $\sim 1/10$  of propane/argon partial pressure in the  $\{\text{C}_3\text{H}_8 + \text{Ar}\}$  gas mixture and Sample 9 shows a  $4/5$  ratio. FE-SEM micrographs of Sample 6 revealed a curved surface topology of VOG coating with the mean height of  $\sim 189\text{ nm}$  (Figure 3A) grown above a bottom buffer layer ( $\sim 42\text{ nm}$ ) (Figure A6 and Table 2). In contrast, the height of the VOG coating of Sample 9 is  $\sim 489\text{ nm}$  and the carbon nanostructures become less curved (Figure 3D). At the partial pressure of propane comparable to the previously described Samples 1–5, shortening the heating time (20 min) and lowering the temperature ( $350\text{ }^\circ\text{C}$ ) leads to a morphology of VOG (Sample 7) that is comparable to Sample 3 (Figure 3B). However, the height of the VOG coating in Sample 7 is smaller ( $\sim 318\text{ nm}$  vs.  $373\text{ nm}$  in Sample 3) and the curved carbon walls are thinner ( $\sim 8\text{ nm}$  vs.  $16\text{ nm}$  in Sample 3) (Table 2). Increased

heating time (60 min) and higher temperature (500 °C) (Sample 8) lead to the formation of VOG morphology with an onion type of carbon nanostructures with the coating height  $\sim 308$  nm (Figure 3C). Although the morphology of VOG in Sample 8 is comparable to Sample 4, the height of the coating in the latter is higher. This demonstrates that the proposed method for coating formation is efficient at lower  $T$ , i.e., 40/450 °C, and shorter operation time (40 min instead of 1 h).

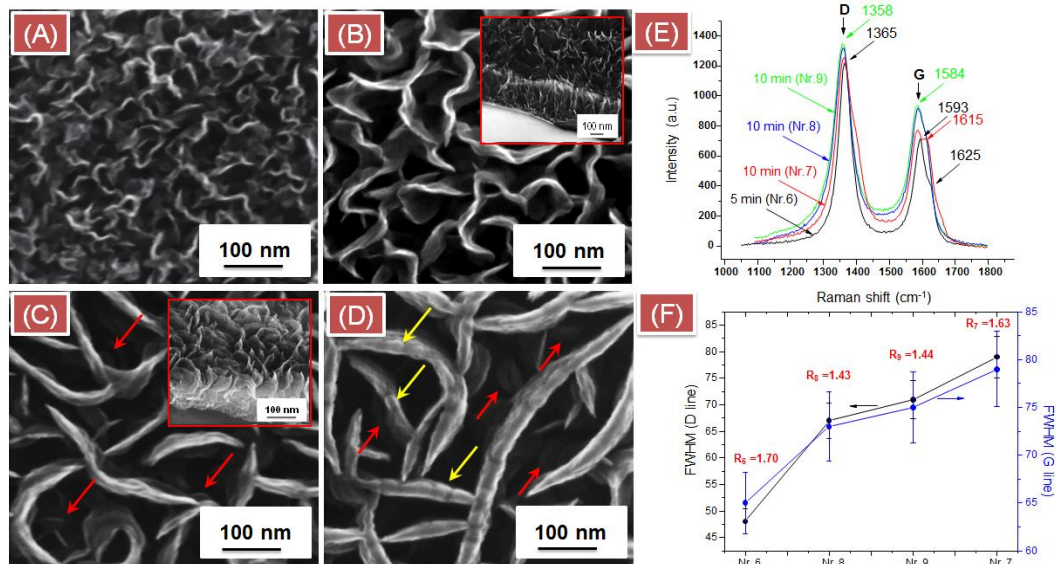


**Figure 3.** (A–D) Representative FE-SEM images of a VOG coating prepared by the ICP CVD roll-to-roll method at technological parameters corresponding to Samples 6–9. (E) Averaged Raman spectra of these VOG coatings (473 nm excitation wavelength, 100× objective, 10 s of integration time). Color coding represents the samples by numbering. (F) Full width at half maximum (FWHM) values of the D and G lines calculated from the averaged Raman spectra. The “R” (in red color) represents the calculated IntD/IntG (peak height) ratio.

Next, we performed the Raman analysis of Samples 6–9 and examined the primary D and G bands and their secondary modes (Figures 3E,F and A7). Each D band of a VOG coating is shifted towards higher frequency by  $\sim 15$  cm<sup>-1</sup> (Sample 6),  $\sim 13$  cm<sup>-1</sup> (Sample 7),  $\sim 10$  cm<sup>-1</sup> (Sample 8) and  $\sim 8$  cm<sup>-1</sup> (Sample 9) (Figure 3E). Each G band also shifted towards higher frequency by  $\sim 12$  cm<sup>-1</sup> (Sample 6),  $\sim 5$  cm<sup>-1</sup> (Samples 7 and 8) and  $\sim 3$  cm<sup>-1</sup> (Sample 9). Sample 6 shows a shoulder at  $\sim 1625$  cm<sup>-1</sup> that is assigned to D' line, indicating a disordered nanocrystalline graphite with small polycrystalline grains (Sample 6). In Sample 7, the D' line appears as a split G peak at  $\sim 1615$  cm<sup>-1</sup>, and in Samples 8 and 9, it causes the broadening of the G mode. The calculated FWHM values of D and G modes are shown in Figure 3F. Both D and G bands in Sample 6 are the narrowest demonstrating that G mode becomes localized on shorter sp<sup>2</sup>-hybridized carbon chains with a sharper length distribution. The IntD/IntG ratio is the highest for this VOG type (Sample 6), demonstrating higher disorder and the decreased number of carbon clusters, which become smaller. In Sample 7, both D and G bands became the broadest with an asymmetrical profile, demonstrating the formation of nanocrystalline graphite with many carbon clusters of different orders and dimensions containing sp<sup>2</sup>-hybridized carbon dimers in an ion-implanted diamond structure. The IntD/IntG ratio of this VOG type (Sample 7) is comparable to that of Sample 6, indicating higher disorder of the carbon network. Therefore, carbon amorphization of highly disordered polycrystalline VOG takes place at lower heating temperature (350 °C) after 20 min of thermal treatment. VOG prepared at higher heating temperature (Sample 8, 500 °C) and longer thermal treatment (60 min instead of 40 min) show the lowest IntD/IntG ratio, indicating clustering of sp<sup>2</sup>-hybridized carbon sites into fairly ordered aromatic rings and increased order of the polycrystalline structure with a smaller number of ordered

hexagons. The IntD/IntG ratio and FWHM values in Sample 8 are comparable to those of Sample 9 (highest partial pressure of propane).

The second order  $G'$ ,  $\{D+G\}$  and  $2D'$  bands are most prominent in Sample 6, confirming the presence of highly disordered polycrystalline nanographitic structure with decreased amount of carbon clusters (Figure A7A). In this sample, the  $G'$  band was strongly shifted towards higher frequency (by  $\sim 11 \text{ cm}^{-1}$ ), indicating pronounced changes in the stacking order of graphene sheets along the  $c$  axis [73] (Figure A7B). In contrast, the  $\{D+G\}$  band was strongly shifted towards lower frequency (by  $\sim 15 \text{ cm}^{-1}$ ) in Samples 7–9, pointing out to the presence of nanocrystalline disordered carbon clusters. The  $2D'$  band was strongly shifted towards higher frequency in all VOG types: by  $\sim 27 \text{ cm}^{-1}$  (Sample 6) and  $\sim 73 \text{ cm}^{-1}$  (Samples 7–9), demonstrating defects introduced in the polycrystalline carbon network.

### 3.3. Effect of Partial Pressure of Nitrogen or Silane at Isothermal (450 °C) Conditions

We applied FE-SEM method in order to characterize the changes in VOG morphology in the  $\{C_3H_8 + Ar + N_2\}$  or  $\{C_3H_8 + Ar + SiH_4\}$  gas mixture by varying the partial pressure of nitrogen or silane (Figure 4A–D and Figure A8). Similarly to the undoped VOG coating (Figure 1C,D), the nitrogen-doped or silicon-doped VOG coating also consists of carbonaceous nanostructures being continuous across surface defects of copper foil substrate with the full area coverage at the centimeter scale (Figure A8A,B,E,F). However, the presence of nitrogen significantly changed the VOG morphology, which acquired a tightly packed form of thick pillars with a mean diameter of  $\sim 50 \text{ nm}$  after preparation in atmosphere at lower  $N_2$  partial pressure (Sample N1) (Figure A8C,D) and  $\sim 90 \text{ nm}$  being formed at higher  $N_2$  partial pressure (Sample N2) (Figure 4A,B).

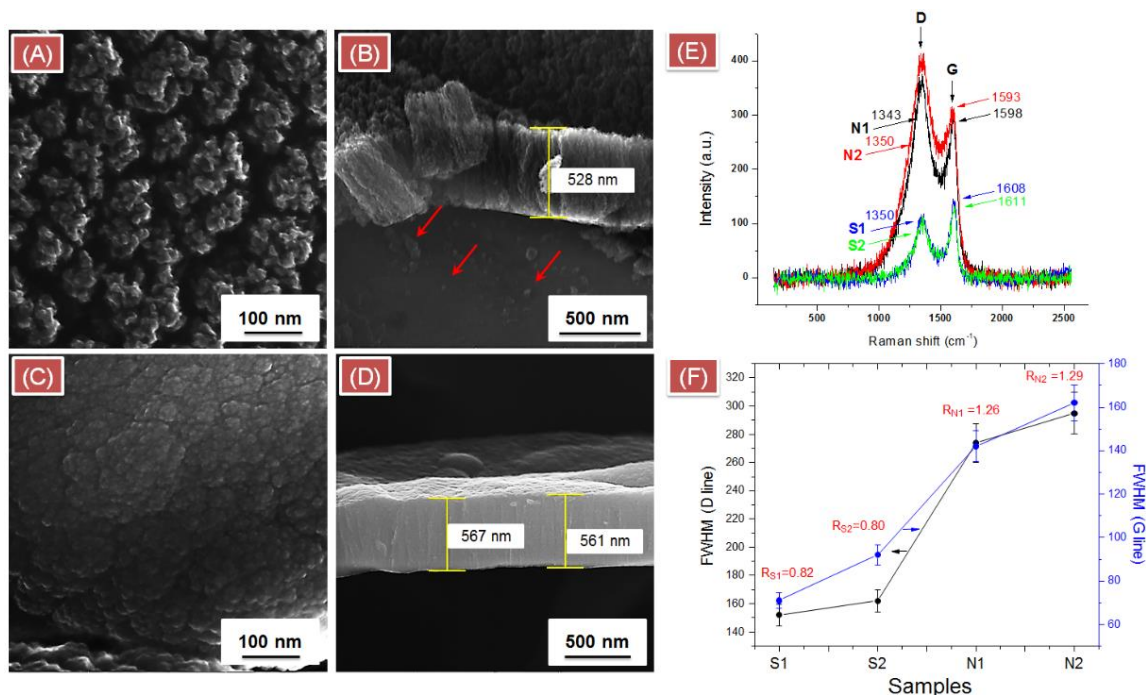


**Figure 4.** (A,B) Representative FE-SEM images of top and cross section views of nitrogen-doped VOG (Sample N2) and (C,D) silicon-doped VOG (Sample S2) prepared by the ICP CVD roll-to-roll technology in the  $\{C_3H_8 + Ar + N_2\}$  gas mixture at 1.0 Pa  $N_2$  partial pressure and  $\{C_3H_8 + Ar + SiH_4\}$  at  $\sim 12.5\%$  (i.e., 100 sccm) of  $SiH_4$  partial pressure, both at 1.5 Pa of total pressure. (E) Averaged Raman spectra of nitrogen-doped VOG (Samples N1 and N2) and silicon-doped VOG (Samples S1 and S2) (473 nm excitation wavelength,  $100\times$  objective, 10 s of integration time). (F) Full width at half maximum (FWHM) values of the D and G bands calculated from the averaged Raman spectra. The “R” (in red color) represents the calculated IntD/IntG (peak height) ratio.

The estimated averaged height of nitrogen-doped VOG coating is ~489 nm (Sample N1, Figure A8C) and ~528 nm (Sample N2, Figure 4A). In FE-SEM images of this type of coating the increased VOG density packing and the vertical orientation of pillars may indicate that the electric field, which directs the growth of nanostructures, can be localized above the substrate during the plasma process [27,77]. At these conditions in atmosphere at lower N<sub>2</sub> partial pressure, VOG pillars were assembled into nanostructures, consisting of agglomerated columns (Figure A8D). In atmosphere at higher N<sub>2</sub> pressure, these VOG pillars fuse and form columns with increased thickness (Figure 4B), thereby enlarging the surface packing area. FE-SEM revealed the presence of excessive amount of nucleation centers in this VOG coating as indicated by red arrows (Figure 4A). Higher N<sub>2</sub> pressure may increase the internal stress arising from the temperature gradients, ion bombardment and lattice mismatch between the copper substrate and graphitic material. Therefore, it may cause defects or buckling in the buffer layer, resulting in an increased number of nucleation sites, which promote the VOG growth and its tighter packing structure [27]. Higher pressure may also increase the step-flow process leading to an increased number of nucleation centers (i.e., Volmer-Weber islands) at the bottom of the copper foil substrate [71]. EDX analysis reveals the presence of nitrogen in these VOG coatings, which increases at higher N<sub>2</sub> partial pressure (Table A1).

In contrast to nitrogen, the presence of silane does not cause the formation of pillars, but a smoothly dense vertically oriented continuous carbonaceous coating (Figure A8G,H and Figure 4C,D). FE-SEM reveals that the surface of a silicon-doped VOG coating is composed of non-uniform tightly packed grains with a mean diameter ~32 nm (Sample S1, Figure A8H) that become larger at twice the higher partial pressure of silane, i.e., ~67 nm (Sample S2, Figure 4D). The overall height of this type of coating is ~497 nm (Sample S1) and ~564 nm (Sample S2), which is comparable to the nitrogen-doped VOG.

EDX analysis of Sample S2 revealed the presence of C (~63 at.%), O (~19 at.%) and Si (~18 at.%) (Figure A9 and Table A1). Similarly to the nitrogen-doped coating, the amount of Si in VOG also increases at higher pressure of silane. The presence of oxygen may point to the soft and porous structure of VOG film [78,79]. On one hand, oxygen may be physisorbed on the VOG surface (the adsorption energy is ~−0.085 eV) and its interaction with the carbon network may occur via the electron transfer reaction from graphene to the O<sub>2</sub> molecule [80]. On the other hand, the O<sub>2</sub> molecule may be chemisorbed on the surface of Si-doped graphene in a parallel direction to the graphene plane, this being the most energetically favorable configuration through the formation of two chemical bonds with the Si atom (adsorption energy is ~−1.439 eV) [80]. The chemisorbed O<sub>2</sub> molecule may be effectively dissociated on Si-doped graphene via cycloaddition, followed by the cleavage of the activated oxygen bond of O<sub>2</sub>. Silicon as a dopant has a larger atomic radius than carbon and oxygen, and may protrude outside of the graphene plane [19]. The Si atom may bind strongly at the defect site because the corresponding diffusion barrier for Si atom is about 80 eV. The O<sub>2</sub> molecule may be placed in a tilted position with the surface being adsorbed over Si atom of the graphene plane. The Si atom may be more inclined in order to provide free electrons to the electron system of graphene and may bind to the sp<sup>3</sup>-hybridized carbon. The presence of SiC is probable because it can be obtained from the mixture consisting of SiH<sub>4</sub> and CH<sub>4</sub> at relatively low temperature (e.g., <450 °C) and also by decomposition due to the mixture of CH<sub>4</sub> and Ar. The presence of silica particles cannot be completely excluded in a silicon-doped VOG film, although silane was diluted in Ar in order to prevent the formation of radicals from silane in plasma. We assumed that in nitrogen-doped VOG, a negligible amount of SiO<sub>2</sub> can be introduced to the VOG from the reaction CVD chamber via the desorption from its walls. According to the Ellingham diagram, Si oxidizes at any oxygen partial pressure higher than ~10<sup>−26</sup> atm at elevated temperatures [81]. The Si impurities in molten Cu metal cannot be separated easily due to the formation of SiO<sub>2</sub> inclusions, which contain some copper oxide regions around them. These impurities may enhance the catalytic activity of the copper substrate in the decomposition of CH<sub>4</sub> [82].

Next, we performed a Raman analysis of nitrogen- and silicon-doped VOG in order to examine the changes in the crystalline and amorphous phases of carbon as a result of doping effect (Figure 4E,F and Figure A10). In contrast to undoped VOG coating (Figures 2E and 3E), Raman spectra of nitrogen- and silicon-doped VOG show broader D and G bands starting to overlap; this is correlated to a distribution of clusters with different orders and dimensions (Figure 4E). The second order  $G'$ ,  $\{D+G\}$  and  $2D'$  bands are more pronounced in a silicon-doped VOG, but they become less defined in Sample N1 and appear as a broad feature from  $\sim 2600$  to  $3300\text{ cm}^{-1}$  in Sample N2, indicating the formation of amorphous carbon (Figure A10A). We suggest that in nitrogen-doped VOG, no transition takes place from  $\alpha$ -C (amorphous carbon) to  $t\alpha$ -C (diamond amorphous carbon) because the G band is not dispersive and not shifted to  $\sim 1570\text{ cm}^{-1}$  (only to  $\sim 1593\text{ cm}^{-1}$ ), and the  $\text{IntD}/\text{IntG}$  ratio is relatively high.

In nitrogen-doped VOG these two modes are stronger than in a silicon-doped coating, indicating the nanocrystalline graphite. The Raman D band of nitrogen-doped VOG at lower  $\text{N}_2$  partial pressure is shifted towards lower frequency (by  $\sim 7\text{ cm}^{-1}$ ), but appears at its characteristic peak position ( $\sim 1350\text{ cm}^{-1}$ ) at higher partial pressure of nitrogen. The D band shift to the lower frequency in Sample N1 may be caused by a decreased number of ordered aromatic rings on passing from nanocrystalline graphite to amorphous  $\alpha$ -C carbon with increasing disorder in the structure because of higher  $\text{IntD}/\text{IntG}$  ratio ( $\sim 1.26$ ). This  $\text{IntD}/\text{IntG}$  ratio is increased in Sample N2 ( $\sim 1.29$ ), implying that the nanocrystalline graphite developed amorphous carbon domains under higher  $\text{N}_2$  partial pressure [83–85], meaning that nitrogen can be mostly incorporated in  $\text{sp}^2$ - and cross-linked  $\text{sp}^3$ -hybridized carbon network [86–88]. Overall, a higher  $\text{IntD}/\text{IntG}$  ratio is accompanied with larger values for the size of graphitic clusters  $L_a$ , demonstrating an increased number of distorted clusters until their closure (Figure A10B). The incorporation of nitrogen into the VOG carbon network may occur via the electron charge transfer from C to N [89]. These nitrogen atoms may inject a pair of electrons into the  $\pi$ -conjugated system and alter the HOMO and LUMO distribution in graphene [90]. The possible binding states in nitrogen-doped VOG may be  $\text{sp}^3$ -hybridized C–N [86] and  $\text{sp}^2$ -hybridized trigonal C–N. Nitrogen atoms may have three  $\text{sp}^2$ -hybridized carbon neighbors in substitutional graphite sites [88]. We may assume the formation of the carbon nitride structure (e.g., theoretically predicted  $\beta$ - $\text{C}_3\text{N}_4$  phase) [84], in which the first nitrogen atoms go into sites where they bond only to aromatic carbon atoms. Some of the N atoms may form a bond to  $\text{sp}^3$ -hybridized carbon when more nitrogen is incorporated into VOG, which is feasible at elevated temperature ( $350$ – $550\text{ }^\circ\text{C}$ ) [85]. At this temperature the tetrahedral component of the C–N bond tends to undergo a transition into a more stable trigonal configuration, characterized by a high level of aromatic electrons available for charge transport. This transition may be accompanied by the transformation to a three-dimensional nitrogen-doped carbon network structure [91]. The carbon lattice network of VOG may be enriched with nitrogen, whereby nitrogen is placed instead of carbon in case of an increased concentration of nitrogen in the reaction chamber [92]. Overall, doping of amorphous carbon layers by nitrogen may lead to a higher electrical conductivity because N acts as a dopant near the edge of the density-of-states in the  $\text{sp}^3$ -hybridized carbon matrix. Previous studies have shown that doping the carbon network with nitrogen may lead to a higher Young's modulus, because N acts to promote the three-dimensional curvature and attachment to the  $\text{sp}^2$ -hybridized carbon clusters [87].

However, in silicon-doped VOG the partial pressure of silane does not change the peak position of the D band ( $\sim 1350\text{ cm}^{-1}$ ), revealing better ordering in the structure. In contrast to nitrogen-doped VOG, doping by silicon may lead to a more developed  $\text{sp}^2$ -hybridized graphitized structure, which may be more enhanced at higher partial pressure of silane, because of the lower  $\text{IntD}/\text{IntG}$  ratio (Figure 4F). In contrast to nitrogen-doped VOG, the decreased  $\text{IntD}/\text{IntG}$  ratio at higher partial pressure of silane and smaller  $L_a$  values demonstrate increased ordering in the structure, with a higher number of less distorted clusters (Figure A10B). In addition, the decrease in the D peak intensity also indicates that the as-grown VOG coating is of higher quality. We can assume that there are no progressively introduced defects into the graphite layer because no softening of the G band takes place, i.e., no dispersion and no shift to the lower frequency range.

We assume that the layer-edge surfaces were not generated by fracture, and that the layer-plane surface was etched and then annealed because the D band did not show a doublet with  $D_1$  ( $\sim 1350\text{ cm}^{-1}$ ) and  $D_2$  ( $\sim 1370\text{ cm}^{-1}$ ) [76]. The presence of oxygen in the gaseous reaction atmosphere led to the higher frequency shift of the G band in both nitrogen- and silicon-doped VOG, but did not change the D band position in a silicon-doped VOG, suggesting the change in the chemical potential and polarizability in the carbonaceous coating. There is no  $D'$  band ( $\sim 1620\text{ cm}^{-1}$ ), which is mainly attributed to the low degree of crystalline structure caused by lower growth temperature, suggesting VOG composed of graphite with higher crystallinity. This crystallinity with higher ordering structure is more pronounced in a silicon-doped VOG. The shift of the G band may indicate the formation of nanocrystalline graphite at the initial nucleation state. However, this shift occurs without the appearance of the  $D'$  band, indicating the formation of larger grains in a polycrystalline structure, which is typical for a large scale CVD graphene films consisting of numerous grain boundaries, in agreement with our SEM observation [93,94].

We suggest that chemical doping of VOG by Si may occur via the substitutional pathway rather than by the surface transfer process. In the substitutional pathway, Si heteroatoms may replace the carbon atoms in the skeleton and break the structure of graphene because the  $\text{IntD}/\text{IntG}$  ratio decreases as a result of the slight local distortions of a graphene lattice induced by the Si atoms embedded in the lattice. In contrast to nitrogen, the incorporation of silicon into the carbon network did not bring new charge carriers, which is consistent with silicon substituting carbon in the trigonal arrangement.

In both nitrogen- and silicon-doped VOG the FWHM value increases with higher partial pressure of nitrogen or silane, pointing to an increased content of  $\text{sp}^2$ -hybridized carbon in VOG after doping (Figure 4F). Notably, the  $\text{sp}^2$ -hybridized carbon consists of parallel graphitic layers with  $\sigma$  planar-bond and  $\pi$ -bond between the layers, giving rise to weak Van-der-Waals forces. Therefore, an increased  $\text{sp}^2$ -hybridized carbon content may lead to the domination of the valence and conduction bands, consisting of the bonding and antibonding  $\pi$ - and  $\pi^*$ - orbitals, resulting in improved electrical conductivity. The degree of  $\text{sp}^2$ -hybridized carbon clustering, but not directly the  $\text{sp}^3$ -hybridized content, may correlate with the optical and mechanical properties of VOG. The clustering of  $\text{sp}^2$ -hybridized carbon sites into fairly ordered aromatic rings may require the conversion of  $\text{sp}^3$ -hybridized carbon sites to  $\text{sp}^2$ -hybridized carbon sites followed by the increase of the  $\text{sp}^2$ -hybridized cluster size, which is mostly pronounced in Samples N1 and N2, but also in Samples S1 and S2, and Samples 4 and 5 (Figure A10B).

#### 3.4. Possible Growth Mechanism of Nitrogen- or Silicon-Doped VOG

The formation of a VOG coating occurs through an interface, which is distinct in structure, composition and mechanical properties from the coating and the substrate. Above the substrate, two distinct regions or layers can be observed. One VOG layer is located immediately above the substrate, i.e., the buffer layer. Another layer rests on top of the initial layer with its interface. The buffer layer may be composed of amorphous carbon and graphitic layering on the surface. Some mismatches in the graphitic layers can also be observed. The upper VOG layer nucleates from carbon onions [95]. Similar to the buffer layer, the onions also serve as active nucleation sites for further VOG growth. The graphene layers grow in tangential direction, naturally leading to a flower shaped structure. The vertical growth may be initiated by the active edges or steps after nucleation. These steps are not straight, but in a round shape and arch upward, playing the same role as the active edges that mediate the VOG growth in the upward direction. Straight edges are closed and may consist of numerous graphene layers. There is a tendency for edge closure of two adjacent graphene layers under high temperature, leading to the natural cessation of the growth.

The VOG growth rate may be closely related to the gas dissociation energy and the formation of reactive  $\text{C}_2$  dimers in plasma. Plasma can produce a relatively larger chemical potential gradient near the surface through ion focusing effects and fast delivery of precursors. The ion bombardment on the surface plays an important role for nucleation by creating active sites for neutral radical bonding [96]. It may also increase the temperature of the top surface layer and the diffusion coefficient due to the

nonuniform electric field on the surface. In the plasma,  $C_3H_8$  undergoes pyrolysis yielding species such as  $C_2H_6$ ,  $C_2H_4$ ,  $C_2H_3$ ,  $C_2H_2$ ,  $CH_4$ ,  $CH_3$ , which decompose into pure carbon and  $H_2$  during the reactions between argon ions and highly energetic electrons in the gas phase [51]. Below the threshold temperature of  $450\text{ }^\circ\text{C}$ , carbon species generated by RF plasma are unable to dissolve into the copper substrate, hydrocarbons are adsorbed on the surface, decomposed by the Cu surface and form graphene. Instead of dissolving and precipitating on the surface of the transition metals, the hydrocarbon precursors may directly dissociate on the surface of Cu, then assemble into graphene structure. Pure carbon and  $H_2$  may be transported towards the copper foil surface resulting in the formation of a carbonaceous coating. A suitable amount of H atoms or OH radicals can etch the amorphous carbon and contribute to the vertically oriented growth of graphene nanostructures. The resulting graphene has a center comprised of C and outer ring, proving the growth is only surface mediated because of the low carbon solubility on Cu substrate [97].

The VOG growth may be considered as a step-flow process on the basis of nucleation at the bottom. At lower temperatures ( $<450\text{ }^\circ\text{C}$ ), graphene may be formed from the carbide surface that is created upon exposure to hydrocarbons through the carbon segregation from bulk to the graphene-carbide interface. The increase in the partial pressure of propane may also increase the nucleation density of graphene on the substrate, thereby causing the formation of multiple graphene domains, and may result in a highly packed polycrystalline graphite nanostructure. The thickness of VOG nanostructures may depend on the number of layers, which nucleate from the bottom. The vertical growth of VOG is controlled via the inductively coupled plasma power and the heating temperature of a copper foil substrate, i.e., determined by the magnitude of the electric field, which directs the growth of nanostructures. Nanostructures become larger when the growth is dominant at the free edges of the graphene, and acquire thicker walls at active steps/edges on their two sides. Higher plasma power may lead to the formation of a denser VOG at a lower temperature ( $<450\text{ }^\circ\text{C}$ ). We assume that smaller and denser VOG can also be grown as a result of increased  $CH_4$  concentration, the density of plasma and number of radicals. The latter may be increased by the presence of silane in the reaction gaseous mixture. In the plasma, silane may react with the carbonaceous species leading to the formation of silicon carbide, carbon and silicon in their pure states. The presence of Ar may promote the formation of  $C_2$  and  $H_2$  and their interaction with silicon and oxygen on the copper substrate surface. Oxygen atoms,  $H_2$  and hydroxyl radicals may etch the amorphous carbon layer and remove the unnecessary nucleation sites, thereby favoring the growth of large area single carbon crystals through the healing of any structural defects occurring during the growth [98].

#### 4. Conclusions

A new method was developed for the mass production of vertically oriented graphene nanostructures (VOG) on a moving copper foil substrate at lower temperature ( $<500\text{ }^\circ\text{C}$ ). This method is based on a unique ICP CVD roll-to-roll technology enabling in situ simultaneous growth and doping of VOG nanostructures by nitrogen or silicon. This technology allows the formation of a uniform 2D VOG coating, which is continuous on the surface defects of the copper foil substrate over the enlarged area, at the centimeter scale. For the first time, the mass production of a VOG coating was enabled by using propane as a carbon source.

A set of technological parameters such as deposition time, gas partial pressure (propane, nitrogen or silane) and heating treatment allow for control over the VOG wall thickness, height of coating and its buffer layer, and for morphology that varies from thin (several nm) curved nanostructures to thicker (tens and hundreds nm) pillars of various packing density. Shorter deposition time (1 min,  $450\text{ }^\circ\text{C}$ —Sample 1, or 10 min,  $350\text{ }^\circ\text{C}$ —Sample 7) leads to thin VOG. Longer deposition time (30 min,  $450\text{ }^\circ\text{C}$ —Sample 5) can cause carbon amorphization and an increased fraction of  $sp^3$ -hybridized carbon, leading to enlargement of VOG nanostructures with developed vertical pillars. Prolonged heat treatment (60 min,  $500\text{ }^\circ\text{C}$ —Sample 8) causes clustering of diamond sites into ordered aromatic rings and increased order in the polycrystalline VOG nanostructure.

In the atmosphere of nitrogen, nanocrystalline VOG develops amorphous carbon domains and nitrogen can be incorporated in aromatic and cross-linked  $sp^3$ -hybridized carbon networks. VOG nanostructures develop a much tighter packing surface topology without interruption of the regular carbonaceous coating, when doped by silicon. This silicon-doped VOG coating acquires a smoother surface and consists of finer grains, which significantly decrease in size at higher concentrations of doped silicon.

We believe that nitrogen-doped VOG coating can find its application in catalysis, while silicon-doped VOG film can be used for Li-ion batteries and supercapacitor applications, enabling better specific capacitance and cycling stability. The proposed ICP CVD roll-to-roll method could be successfully extended to the mass production of VOG doped with other materials in a single step procedure, thereby significantly advancing VOG charge carrier properties.

**Author Contributions:** Conceptualization, E.K., V.S., A.B., N.K. and V.L.; methodology, P.R., L.M. and D.R.; validation, D.R. and I.M.; formal analysis, D.R.; investigation, P.R., D.R. and I.M.; data curation, P.R. and L.M., D.R. and I.M.; writing—original draft preparation, D.R.; writing—review and editing, D.R., V.L., I.M. and V.M.; supervision, V.L.; project administration, V.S. and V.L.; funding acquisition, V.L., D.R. and V.M.

**Funding:** This research was funded by the Belarusian Republican Foundation for Fundamental Research under grant agreement N 16-3041 57 031.00. The financial support to conduct FE-SEM measurements at the Charles University of Prague was provided by the CERIC-ERIC European Consortium under grant agreement Nr. 20177024.

**Acknowledgments:** We appreciate the scientists from the scientific-technical center “Belmicrosystems” (Minsk, Belarus) for the EDX measurements and discussions of obtained results.

**Conflicts of Interest:** The authors declare no conflict of interest.

## Appendix A

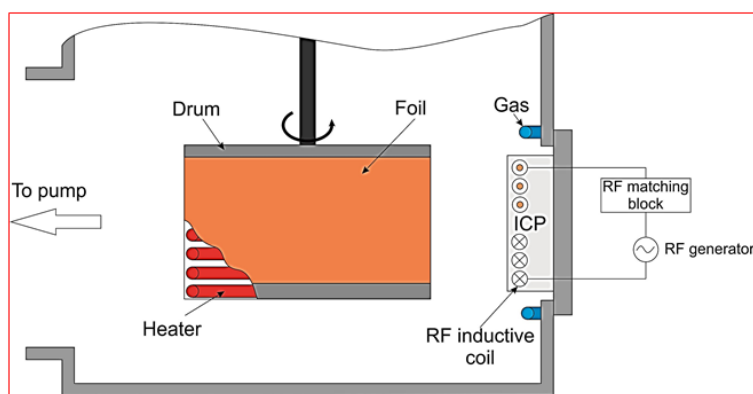


**Figure A1.** Schematic illustration of an inductively coupled plasma chemical vapor deposition (ICP CVD) system coupled to a roll-to-roll (RtR) apparatus, i.e., new ICP CVD Roll-to-Roll technology, which was used for the formation of vertically oriented graphene (VOG) nanostructures on a moving copper foil substrate. This system was connected to a power source, a mass flow controller (Pneucleus Technologies LLC, Hollis, NH, USA), two gas inlets, a radio frequency (RF) generator (13.56 MHz) and a matching block (MB), a drum and a heater designed by IZOVAC TECHNOLOGIES Ltd. The following abbreviations were used:

- ICP—the source of inductively coupled plasma;
- RF generator—a radio frequency signal generator to be used for the plasma process;
- RF matching block—a matching unit aiming at transmatch of output resistance of a high frequency generator with load impedance. This unit was connected to the circuit between a technological device and a transmission line of the generator.
- Gas—a gas inlet for the delivery of a gaseous mixture into the reactor interior;
- Drum—a rotating sample holder to fix the copper foil;
- Heater—a system consisting of electrodes to heat a sample to a desired temperature.

In the ICP CVD system, high vacuum pumping was conducted by a turbomolecular pump, Edwards STP-iXA3306 coupled to a mechanical unit Edwards E2M40 (Edwards Russia, Khimki, Russian). The total working pressure in a chamber was up to 1.5 Pa and the residual pressure was  $\sim 8 \times 10^{-4}$  Pa.

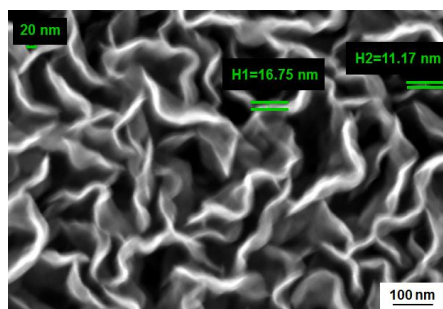


**Figure A2.** Representative FE-SEM image of VOG nanostructures, which were grown on the moving copper foil substrate by using a ICP CVD roll-to-roll method at the following technological parameters: deposition time: 5 min, partial pressure of propane: 2/5 in gas  $\{C_3H_8 + Ar\}$  mixture and heating treatment: 40 min at 450 °C.

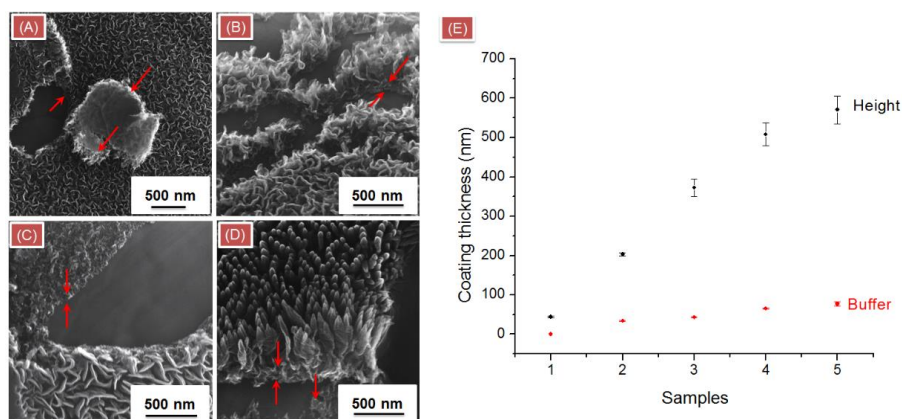


**Figure A3.** (A–D) Representative FE-SEM images of VOG coatings prepared on the copper foil substrate at deposition time: 1 min (A), 5 min (B), 15 min (C) and 30 min (D), and heating treatment: 40 min at 450 °C at 2/5 partial pressure of propane in  $\{C_3H_8 + Ar\}$  gas mixture. Red arrows point to the presence of a bottom buffer layer. (E) Calculated values of the overall height of a VOG coating and its buffer layer thickness obtained from the FE-SEM images. In the plot, the numbers along the x axis indicate the VOG samples.

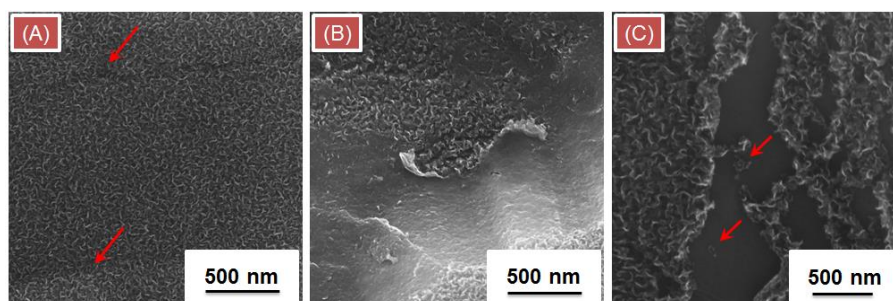


**Figure A4.** (A–C) Representative FE-SEM images of VOG coatings prepared on the copper foil substrate after 1 min of deposition time and heating treatment: 40 min at 450 °C at 2/5 partial pressure of propane in  $\{C_3H_8 + Ar\}$  gas mixture. Red arrows in (A) point to the defects of copper foil caused during the industrial manufacturing process and in (C) to the VOG nucleation centers.

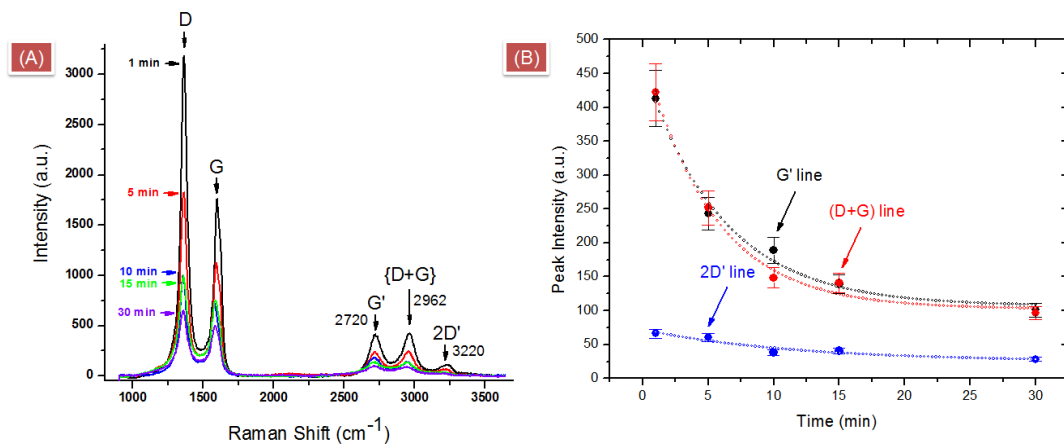


**Figure A5.** (A) Averaged Raman spectra of VOG coatings (Samples 1–5) measured at 473 nm excitation wavelength (100× objective and 10 s of integration time). (B) Peak intensity values of G', {D+G} and 2D' Raman secondary order modes versus deposition time from 1 to 30 min (Samples 1–5).

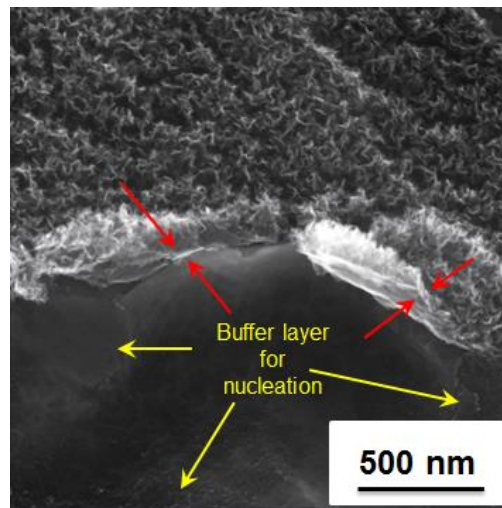


**Figure A6.** Representative FE-SEM image of VOG (Sample 6) prepared by the ICP CVD roll-to-roll technology.

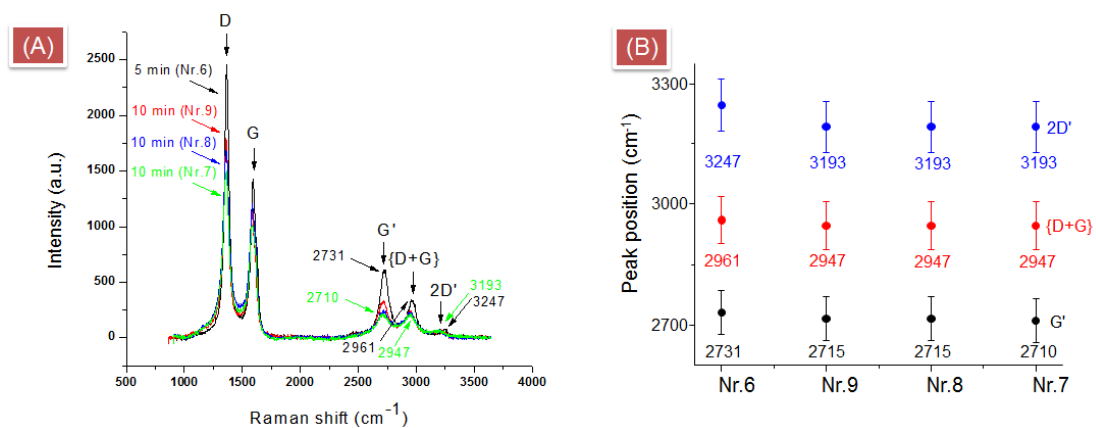


**Figure A7.** (A) Averaged Raman spectra of VOG Samples 6–9 and (B) peak positions of G', {D+G} and 2D' Raman secondary order modes of these samples.

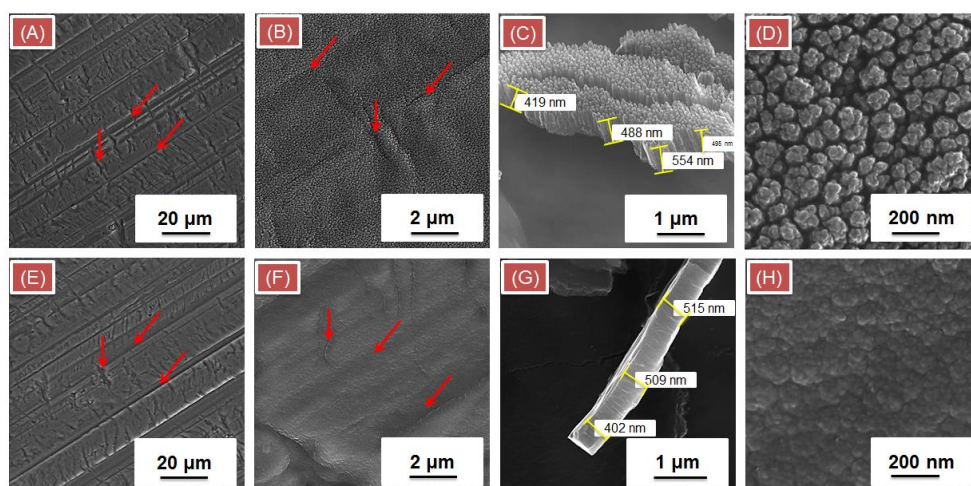


**Figure A8.** (A–D) Representative FE-SEM images of nitrogen-doped VOG coating prepared by the ICP CVD roll-to-roll technology at 0.5 Pa partial pressure of  $N_2$  in  $\{C_3H_8 + Ar + N_2\}$  gas mixture (Sample N1). (E–H) Representative FE-SEM images of silicon-doped VOG at  $\frac{1}{4}$  partial pressure of  $SiH_4$  in  $\{C_3H_8 + Ar + SiH_4\}$  gas mixture (Sample S1).

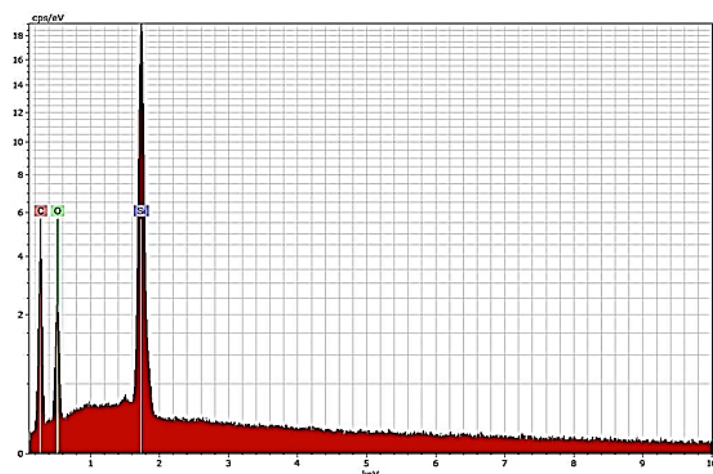


**Figure A9.** EDX spectrum of silicon-doped VOG (Sample S2) measured without Cu foil substrate.

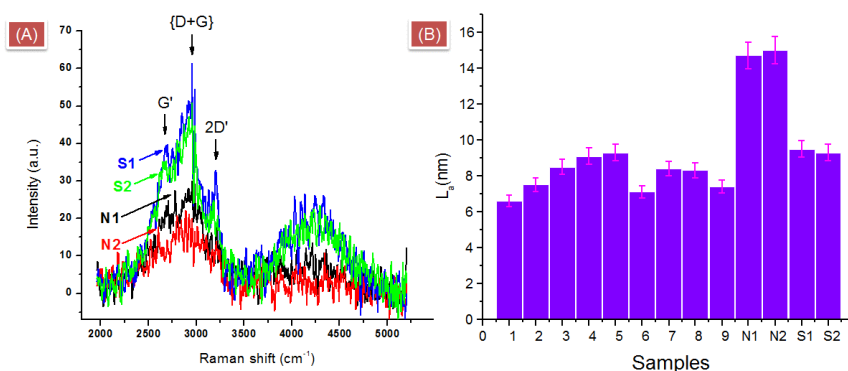


**Figure A10.** (A) Averaged Raman spectra of nitrogen-doped (Samples N1 and N2) and silicon-doped (Samples S1 and S2) VOG coatings obtained at 473 nm excitation wavelength (10 s of integration time and  $100\times$  objective). (B) Calculated values of nanographite size ( $L_a$ , nm) of all types of VOG coatings by using the  $IntD/IntG$  ratio of most prominent D and G Raman bands. The numbers (1–9), N1 and N2, S1 and S2 along the x axis indicate VOG samples.

**Table A1.** Elemental composition of undoped, nitrogen- (Samples N1 and N2) and silicon-doped VOG coatings (Samples S1 and S2) obtained from the EDX spectra.

Sample	Element	Atomic Number	Series	Norm. C [wt.%]	Atom. C [at.%]	Error [wt.%]
Undoped	C	6	K-series	84	87	10
	O	8	K-series	16	12	3
N1	C	6	K-series	65	70	8
	N	7	K-series	18	17	
	O	8	K-series	15	13	3
N2	C	6	K-series	57	62	7
	N	7	K-series	25	24	5
	O	8	K-series	17	14	3
S1	C	6	K-series	54	64	2
	O	8	K-series	31	28	1
	Si	14	K-series	15	8	0.2
S2	C	6	K-series	48	63	7
	O	8	K-series	19	19	3
	Si	14	K-series	33	18	2

Undoped VOG were prepared by ICP CVD roll-to-roll technology after 10 min of deposition time and 45 min of heating at 450 °C and 1.0 Pa of total pressure.

## References

- Prischepa, S.L.; Danilyuk, A.L.; Prudnikava, A.L.; Komissarov, I.V.; Labunov, V.A.; Yanushkevich, K.I.; Normand, F.L. Magnetic properties of nanocomposites based on magnetically functionalized carbon nanotubes. In *Nanomagnetism*; Gonzalez Estevez, J.M., Ed.; One Central Press (OCP): Cheshire, UK, 2014; pp. 227–245.
- Labunov, V.; Prudnikava, A.; Bushuk, S.; Filatov, S.; Shulitski, B.; Tay, B.K.; Shaman, Y.; Basaev, A. Femtosecond laser modification of an array of vertically aligned carbon nanotubes intercalated with Fe phase nanoparticles. *Nanoscale Res. Lett.* **2013**, *8*, 375. [[CrossRef](#)]
- Labunov, V.A.; Danilyuk, A.L.; Prudnikava, A.L.; Komissarov, I.; Shulitski, B.G.; Speisser, C.; Antoni, F.; Le, F.; Prischepa, S.L. Microwave absorption in nanocomposite material of magnetically functionalized carbon nanotubes. *J. Appl. Phys.* **2012**, *112*, 24302–241107. [[CrossRef](#)]
- Labunov, V.A.; Basaev, A.S.; Shulitski, B.G.; Shaman, Y.P.; Komissarov, I.; Prudnikava, A.L.; Tay, B.K.; Shakerzadeh, M. Growth of few-wall carbon nanotubes with narrow diameter distribution over Fe-Mo-MgO catalyst by methane/acetylene catalytic decomposition. *Nanoscale Res. Lett.* **2012**, *7*, 102. [[CrossRef](#)]
- Labunov, V.; Shulitski, B.; Prudnikava, A.; Basaev, A. Multilevel composite nanostructures based on the arrays of vertically aligned carbon nanotubes and planar graphite layers. *Phys. Status Solidi* **2011**, *208*, 453–458. [[CrossRef](#)]
- Navitski, A.; Müller, G.; Sakharuk, V.; Prudnikava, A.L.; Shulitski, B.G.; Labunov, V.A. Efficient high-current field emission from arrays of carbon nanotube columns. *J. Vac. Sci. Technol. B* **2010**, *28*, C2B14–19. [[CrossRef](#)]
- Novoselov, K.S.; Geim, A.K.; Morozov, S.V.; Jiang, D.; Zhang, Y.; Dubonos, S.V.; Grigorieva, I.V.; Firsov, A.A. Electric field effect in atomically thin carbon films. *Science* **2004**, *306*, 666–669. [[CrossRef](#)]
- Novoselov, K.S.; Jiang, D.; Schedin, F.; Booth, T.; Khotkevich, V.V.; Morozov, S.V.; Geim, A.K. Two-dimensional atomic crystals. *Proc. Natl. Acad. Sci. USA* **2005**, *102*, 10451–10453. [[CrossRef](#)] [[PubMed](#)]
- Bo, Z.; Mao, S.; Han, Z.J.; Cen, K.; Chen, J.; Ostrikov, K. Emerging energy and environmental applications of vertically-oriented graphenes. *Chem. Soc. Rev.* **2015**, *44*, 2108–2121. [[CrossRef](#)]
- Lee, H.C.; Bong, H.; Yoo, M.S.; Jo, M.; Cho, K. Copper-vapor-assisted growth and defect-healing of graphene on copper surfaces. *Small* **2018**, *14*, e1801181. [[CrossRef](#)]
- Song, Y.; Luo, Y.; Zhu, C.; Li, H.; Du, D.; Lin, Y. Recent advances in electrochemical biosensors based on graphene two-dimensional nanomaterials. *Biosens. Bioelectron.* **2016**, *76*, 195–212. [[CrossRef](#)] [[PubMed](#)]
- Torres, T. Graphene chemistry. *Chem. Soc. Rev.* **2017**, *46*, 4385–4386. [[CrossRef](#)]

13. Solís-Fernández, P.; Bissett, M.; Ago, H. Synthesis, structure and applications of graphene-based 2D heterostructures. *Chem. Soc. Rev.* **2017**, *46*, 4572–4613. [[CrossRef](#)] [[PubMed](#)]
14. Cho, D.; Kim, M.; Hwang, J.; Park, J.H.; Joo, Y.L.; Jeong, Y.A. Tremella-like nanostructure of silicon@void@graphene-like nanosheets composite as an anode for Lithium-ion batteries. *Nanoscale Res. Lett.* **2016**, *11*, 204. [[CrossRef](#)]
15. Luo, B.; Zhi, L. Design and construction of three dimensional graphene-based composites for Lithium ion battery applications. *Energy Environ. Sci.* **2015**, *8*, 456–477. [[CrossRef](#)]
16. Bundaleska, N.; Henriques, J.; Abrashev, M.; Botelho do Rego, A.M.; Ferraria, A.M.; Almeida, A.; Dias, F.M.; Valcheva, E.; Arnaudov, B.; Upadhyay, K.K.; et al. Large-scale synthesis of free-standing N-doped graphene using microwave plasma. *Sci. Rep.* **2018**, *8*, 12595. [[CrossRef](#)]
17. Kong, X. Metal-free Si-doped graphene: A new and enhanced anode material for Li ion battery. *J. Alloy. Compd.* **2016**, *687*, 534–540. [[CrossRef](#)]
18. Xiong, D.; Li, X.; Bai, Z.; Shan, H.; Fan, L.; Wu, C.; Li, D.; Lu, S. Superior cathode performance of nitrogen-doped graphene frameworks for Lithium ion batteries. *ACS Appl. Mater. Interfaces* **2017**, *9*, 10643–10651. [[CrossRef](#)]
19. Esrafil, M.D.; Saeidi, N.; Nematollahi, P. Si-doped graphene: A promising metal-free catalyst for oxidation of SO<sub>2</sub>. *Chem. Phys. Lett.* **2016**, *649*, 37–43. [[CrossRef](#)]
20. Liu, Y.; Miao, X.; Fang, J.; Zhang, X.; Chen, S.; Li, W.; Feng, W.; Chen, Y.; Wang, W.; Zhang, Y. Layered-MnO<sub>2</sub> nanosheet grown on nitrogen-doped graphene template as a composite cathode for flexible solid-state asymmetric supercapacitor. *ACS Appl. Mater. Interfaces* **2016**, *8*, 5251–5260. [[CrossRef](#)]
21. Sheng, L.; Jiang, L.; Wei, T.; Fan, Z. High volumetric energy density asymmetric supercapacitors based on well-balanced graphene and graphene-MnO<sub>2</sub> electrodes with densely stacked architectures. *Small* **2016**, *12*, 5217–5227. [[CrossRef](#)] [[PubMed](#)]
22. Xue, Y.; Wu, B.; Bao, Q.; Liu, Y. Controllable synthesis of doped graphene and its applications. *Small* **2014**, *10*, 2975–2991. [[CrossRef](#)] [[PubMed](#)]
23. Komissarov, I.V.; Kovalchuk, N.G.; Labunov, V.A.; Girel, K.V.; Korolik, O.V.; Tivanov, M.S.; Lazauskas, A.; Andrulevičius, M.; Tamulevičius, T.; Grigaliūnas, V.; et al. Nitrogen-doped twisted graphene grown on copper by atmospheric pressure CVD from a decane precursor. *Beilstein J. Nanotechnol.* **2017**, *8*, 145–158. [[CrossRef](#)] [[PubMed](#)]
24. Li, X.; Colombo, L.; Ruoff, R.S. Synthesis of graphene films on copper foils by chemical vapor deposition. *Adv. Mater.* **2016**, *28*, 6247–6252. [[CrossRef](#)]
25. Fang, W.; Hsu, A.L.; Song, Y.; Kong, J. A review of large-area bilayer graphene synthesis by chemical vapor deposition. *Nanoscale* **2015**, *7*, 20335–20351. [[CrossRef](#)]
26. Chen, Z.; Zhang, W.; Palma, C.-A.; Rizzini, A.L.; Liu, B.; Abbas, A.; Richter, N.; Martini, L.; Wang, X.-Y.; Cavani, N.; et al. Synthesis of graphene nanoribbons by ambient-pressure chemical vapor deposition and device integration. *J. Am. Chem. Soc.* **2016**, *138*, 15488–15496. [[CrossRef](#)] [[PubMed](#)]
27. Lee, H.-C. Review of inductively coupled plasmas: Nano-applications and bistable hysteresis physics. *Appl. Phys. Rev.* **2018**, *5*, 011108. [[CrossRef](#)]
28. Levchenko, I.; Ostrikov, K.; Zheng, J.; Li, X.; Keidard, M.; Teoe, K.B.K. Scalable graphene production: Perspectives and challenges of plasma applications. *Nanoscale* **2016**, *8*, 10511–10527. [[CrossRef](#)] [[PubMed](#)]
29. Ye, X.; Zhou, H.; Levchenko, I.; Bazaka, K.; Xu, S.; Xiao, S. Low-temperature synthesis of graphene by ICP-Assisted amorphous carbon sputtering. *ChemistrySelect* **2018**, *3*, 8779–8785. [[CrossRef](#)]
30. Zheng, S.; Zhong, G.; Wu, X.; D’Arsiè, L.; Robertson, J. Metal-catalyst-free growth of graphene on insulating substrates by ammonia-assisted microwave plasma-enhanced chemical vapor deposition. *RSC Adv.* **2017**, *7*, 33185–33193. [[CrossRef](#)]
31. Quan, B.; Meng, Y.; Li, L.; Yao, Z.; Liu, Z.; Wang, K.; Wei, Z.; Gu, C.; Li, J. Vertical few-layer graphene/metalized Si-nanocone arrays as 3D electrodes for solid-state supercapacitors with large areal capacitance and superior rate capability. *Appl. Surf. Sci.* **2017**, *404*, 238–245. [[CrossRef](#)]
32. Yivlialin, R.; Bussetti, G.; Duò, L.; Yu, F.; Galbiati, M.; Camilli, L. CVD Graphene/Ni interface evolution in sulfuric electrolyte. *Langmuir* **2018**, *34*, 3413–3419. [[CrossRef](#)] [[PubMed](#)]

33. Pu, N.-W.; Shi, G.-N.; Liu, Y.-M.; Sun, X.; Chang, J.-K.; Sun, C.-L.; Ger, M.-D.; Chen, C.-Y.; Wang, P.-C.; Peng, Y.-Y.; et al. Graphene grown on stainless steel as a high-performance and ecofriendly anti-corrosion coating for polymer electrolyte membrane fuel cell bipolar plates. *J. Power Sources* **2015**, *282*, 248–256. [[CrossRef](#)]
34. Ghaemi, F.; Abdullah, L.C.; Tahir, P.M.; Yunus, R. Synthesis of different layers of graphene on stainless steel using the CVD method. *Nanoscale Res. Lett.* **2016**, *11*, 506. [[CrossRef](#)] [[PubMed](#)]
35. Gullapalli, H.; Reddy, A.L.M.; Kilpatrick, S.; Dubey, M.; Ajayan, P.M. Graphene growth via carburization of stainless steel and application in energy storage. *Small* **2011**, *7*, 1697–1700. [[CrossRef](#)] [[PubMed](#)]
36. Shelk, M.V.; Gullapalli, H.; Kalaga, K.; Rodrigues, M.-T.F.; Devarapalli, R.R.; Vajtai, R.; Ajayan, P.M. Facile synthesis of 3D anode assembly with Si nanoparticles sealed in highly pure few layer graphene deposited on porous current collector for long life Li-Ion battery. *Adv. Mater. Interfaces* **2017**, *4*, 1601043. [[CrossRef](#)]
37. Kato, R.; Minami, S.; Koga, Y.; Hasegawa, M. High growth rate chemical vapor deposition of graphene under low pressure by RF plasma assistance. *Carbon* **2016**, *96*, 1008–1013. [[CrossRef](#)]
38. Manikandan, A.; Lee, L.; Wang, Y.-C.; Chen, C.-W.; Chen, Y.-Z.; Medina, H.; Tseng, J.-Y.; Wang, Z.M.; Chueh, Y.-L. Graphene-coated copper nanowire networks as a highly stable transparent electrode in harsh environments toward efficient electrocatalytic hydrogen evolution reactions. *J. Mater. Chem. A* **2017**, *5*, 13320–13328. [[CrossRef](#)]
39. Griep, M.H.; Tumlin, T.M.; Smith, J.T.; Oida, S.; Sano, T.; Demaree, D.; Dimitrakopoulos, C. Enhanced quality CVD-grown graphene via a double-plateau copper surface planarization methodology. *Cryst. Growth Des.* **2017**, *17*, 5725–5731. [[CrossRef](#)]
40. Ago, H.; Ohta, Y.; Hibino, H.; Yoshimura, D.; Takizawa, R.; Uchida, Y.; Tsuji, M.; Okajima, T.; Mitani, H.; Mizuno, S. Growth dynamics of single-layer graphene on epitaxial Cu surfaces. *Chem. Mater.* **2015**, *27*, 5377–5385. [[CrossRef](#)]
41. Ajejas, F.; Gudín, A.; Guerrero, R.; Barcelona, A.A.; Diez, J.M.; de Melo Costa, L.; Olleros, P.; Niño, M.A.; Pizzini, S.; Vogel, J.; et al. Unraveling Dzyaloshinskii–Moriya interaction and chiral nature of graphene/cobalt interface. *Nano Lett.* **2018**, *18*, 5364–5372. [[CrossRef](#)] [[PubMed](#)]
42. Zhang, D.; Xie, F.; Lin, P.; Choy, W.C.H. Al-TiO<sub>2</sub> composite-modified single-layer graphene as an efficient transparent cathode for organic solar cells. *ACS Nano* **2013**, *7*, 1740–1747. [[CrossRef](#)]
43. Verguts, K.; Vermeulen, B.; Vrancken, N.; Schouteden, K.; Van Haesendonck, C.; Huyghebaert, C.; Heyns, M.; De Gendt, S.; Brems, S. Epitaxial Al<sub>2</sub>O<sub>3</sub>(0001)/Cu(111) template development for CVD graphene growth. *J. Phys. Chem. C* **2016**, *120*, 297–304. [[CrossRef](#)]
44. Nam, J.; Kim, D.-C.; Yun, H.; Shin, D.H.; Nam, S.; Lee, W.K.; Hwang, J.Y.; Lee, S.W.; Weman, H.; Kim, K.S. Chemical vapor deposition of graphene on platinum: Growth and substrate interaction. *Carbon* **2017**, *111*, 733–740. [[CrossRef](#)]
45. Babenko, V.; Murdock, A.T.; Koós, A.A.; Britton, J.; Crossley, A.; Holdway, P.; Moffat, J.; Huang, J.; Alexander-Webber, J.A.; Nicholas, R.J.; et al. Rapid epitaxy-free graphene synthesis on silicidated polycrystalline platinum. *Nat. Commun.* **2015**, *6*, 7536. [[CrossRef](#)]
46. Feng, X.; Wu, J.; Bell, A.T.; Salmeron, M. An atomic-scale view of the nucleation and growth of graphene islands on Pt surfaces. *J. Phys. Chem. C* **2015**, *119*, 7124–7129. [[CrossRef](#)]
47. Li, M.; Liu, D.; Wei, D.; Song, X.; Wei, D.; Wee, A.T.S. Controllable synthesis of graphene by plasma-enhanced chemical vapor deposition and its related applications. *Adv. Sci.* **2016**, 1600003. [[CrossRef](#)]
48. Aliofkhazraei, M.; Ali, N.; Milne, W.I.; Ozkan, C.S.; Miture, S.; Gervasoni, J.L. *Graphene Science Handbook: Fabrication Methods*, 1st ed.; CRC Press, Taylor & Francis Group: Abingdon, UK, 2016; pp. 35–715.
49. Chan, S.-H.; Chen, S.-H.; Lin, W.-T.; Li, M.-C.; Lin, Y.-C.; Kuo, C.-C. Low-temperature synthesis of graphene on Cu using plasma-assisted thermal chemical vapor deposition. *Nanoscale Res. Lett.* **2013**, *8*, 285–290. [[CrossRef](#)] [[PubMed](#)]
50. Redekop, E.A.; Saerens, S.; Galvita, V.V.; González, I.P.; Sabbe, M.; Bliznuk, V.; Reyniers, M.-F.; Marin, G.B. Early stages in the formation and burning of graphene on a Pt/Mg(Al)O<sub>x</sub> dehydrogenation catalyst: A temperature- and time-resolved study. *J. Catal.* **2016**, *344*, 482–495. [[CrossRef](#)]
51. Descamps, C.; Vignoles, G.L.; Féron, O.; Langlais, F.; Lavenac, J. Correlation between homogeneous propane pyrolysis and pyrocarbon deposition. *J. Electrochem. Soc.* **2001**, *148*, C695–C708. [[CrossRef](#)]

52. Wassei, J.K.; Mecklenburg, M.; Torres, J.A.; Fowler, J.D.; Regan, B.C.; Kaner, R.B.; Weiller, B.H. Chemical vapor deposition of graphene on copper from methane, ethane and propane: Evidence for bilayer selectivity. *Small* **2012**, *8*, 1415–1422. [[CrossRef](#)]
53. Chen, J.; Bo, Z.; Lu, G. *Vertically-Oriented Graphene, PECVD Synthesis and Applications*; Springer: Cham, Switzerland, 2015. [[CrossRef](#)]
54. Zhang, Z.; Lee, C.-S.; Zhang, W. Vertically aligned graphene nanosheet arrays: Synthesis, properties and applications in electrochemical energy conversion and storage. *Adv. Energy Mater.* **2017**, *7*, 1700678. [[CrossRef](#)]
55. Wei, D.; Peng, L.; Li, M.; Mao, H.; Niu, T.; Han, C.; Chen, W.; Wee, A.T.S. Low temperature critical growth of high quality nitrogen doped graphene on dielectrics by plasma-enhanced chemical vapor deposition. *ACS Nano* **2015**, *9*, 164–171. [[CrossRef](#)] [[PubMed](#)]
56. Seo, D.H.; Kumar, S.; Rider, A.E.; Han, Z.; Ostrikov, K. Deterministic control of structural and optical properties of plasma-grown vertical graphene nanosheet networks via nitrogen gas variation. *Opt. Mater. Express* **2012**, *2*, 700–707. [[CrossRef](#)]
57. Luo, B.; Whelan, P.R.; Shivayogimath, A.; Mackenzie, D.M.A.; Bøggild, P.; Booth, T.J. Copper oxidation through nucleation sites of chemical vapor deposited graphene. *Chem. Mater.* **2016**, *28*, 3789–3795. [[CrossRef](#)]
58. Li, P.; Li, Z.; Yang, J. Dominant kinetic pathways of graphene growth in chemical vapor deposition: The role of hydrogen. *J. Phys. Chem. C* **2017**, *121*, 25949–25955. [[CrossRef](#)]
59. Wang, X.; Sun, G.; Routh, P.; Kim, D.-H.; Huang, W.; Chen, P. Heteroatom-doped graphene materials: Syntheses, properties and applications. *Chem. Soc. Rev.* **2014**, *43*, 7067–7098. [[CrossRef](#)] [[PubMed](#)]
60. Pham, P.V. A Library of doped-graphene images via transmission electron microscopy. *J. Carbon Res.* **2018**, *4*, 34. [[CrossRef](#)]
61. Chen, Y.; Liu, Y.-J.; Wang, H.-X.; Zhao, J.-X.; Cai, Q.-H.; Wang, X.-Z.; Ding, Y.-H. Silicon-doped graphene: AN effective and metal-free catalyst for NO reduction to N<sub>2</sub>O? *ACS Appl. Mater. Interfaces* **2013**, *5*, 5994–6000. [[CrossRef](#)]
62. Wang, H.; Zhou, Y.; Wu, D.; Liao, L.; Zhao, S.L.; Peng, H.L.; Liu, Z.F. Synthesis of boron-doped graphene monolayers using the sole solid feedstock by chemical vapor deposition. *Small* **2013**, *9*, 1316–1320. [[CrossRef](#)] [[PubMed](#)]
63. Peyghan, A.A.; Rastegar, S.F.; Hadipour, N.L. DFT study of NH<sub>3</sub> adsorption on pristine, Ni-and Si-doped graphynes. *Phys. Lett. A* **2014**, *378*, 2184–2190. [[CrossRef](#)]
64. Lv, R.; dos Santos, M.C.; Antonelli, C.; Feng, S.; Fujisawa, K.; Berkdemir, A.; Cruz-Silva, R.; Elías, A.L.; Perea-Lopez, N.; López-Urías, F.; et al. Large-area Si-doped graphene: Controllable synthesis and enhanced molecular sensing. *Adv. Mater.* **2014**, *26*, 7593–7599. [[CrossRef](#)]
65. Wang, Z.; Li, P.; Chen, Y.; Liu, J.; Zhang, W.; Guo, Z.; Dong, M.; Li, Y. Synthesis, characterization and electrical properties of silicon-doped graphene films. *J. Mater. Chem. C* **2015**, *3*, 6301–6306. [[CrossRef](#)]
66. Cuxart, M.G.; Šics, I.; Goñi, A.R.; Pach, E.; Sauthier, G.; Paradinas, M.; Foerster, M.; Aballe, L.; Fernandez, H.M.; Carlino, V.; Pellegrin, E. Inductively coupled remote plasma-enhanced chemical vapor deposition (rPE-CVD) as a versatile route for the deposition of graphene micro- and nanostructures. *Carbon* **2017**, *117*, 331–342. [[CrossRef](#)]
67. Chen, J.; Bo, Z.; Lu, G. PECVD Synthesis of Vertically-Oriented Graphene: Precursor and Temperature Effects. In *Vertically Oriented Graphene*; ebook; Springer: Cham, Switzerland, 2015; pp. 35–54. [[CrossRef](#)]
68. Naghdi, S.; Rhee, K.Y.; Park, S.J. A catalytic, catalyst-free, and Roll-to-Roll production of graphene via chemical vapor deposition: Low temperature growth. *Carbon* **2018**, *127*, 1–12. [[CrossRef](#)]
69. Caçado, L.; Takai, K.; Enoki, T.; Endo, M.; Kim, Y.A.; Mizusaki, H.; Jorio, A.; Coelho, L.N.; Magalhães-Paniago, R.; Pimenta, M.A. General equation for the determination of the crystallite size La of nanographite by Raman spectroscopy. *Appl. Phys. Lett.* **2006**, *88*, 163106. [[CrossRef](#)]
70. Li, X.; Cai, W.; An, J.; Kim, S.; Nah, J.; Yang, D.; Piner, R.; Velamakanni, A.; Jung, I.; Tutuc, E.; et al. Large-area synthesis of high-quality and uniform graphene films on copper foils. *Science* **2009**, *324*, 1312–1314. [[CrossRef](#)]
71. Levine, M.S.; Golovin, A.A.; Volpert, V.A. Step-flow growth of a crystal surface by Lévy flights. *Eur. Phys. Lett.* **2008**, *82*, 28007. [[CrossRef](#)]
72. Yakobson, B.I.; Brabec, C.J.; Bernholc, J. Nanomechanics of carbon tubes: Instabilities beyond linear response. *Phys. Rev. Lett.* **1996**, *76*, 2511–2514. [[CrossRef](#)]

73. Cançado, L.G.; Jorio, A.; Ferreira, E.H.M.; Stavale, F.; Achete, C.A.; Capaz, R.B.; Moutinho, M.V.O.; Lombardo, A.; Kulmala, T.S.; Ferrari, A.C. Quantifying defects in graphene via Raman spectroscopy at different excitation energies. *Nano Lett.* **2011**, *11*, 3190–3196. [[CrossRef](#)] [[PubMed](#)]
74. Ferreira, E.H.M.; Moutinho, M.V.O.; Stavale, F.; Lucchese, M.M.; Capaz, R.B.; Achete, C.A.; Jorio, A. Evolution of the Raman spectra from single-, few-, and many-layer graphene with increasing disorder. *Phys. Rev. B* **2010**, *82*, 125429. [[CrossRef](#)]
75. Ferrari, A.C.; Robertson, J. Interpretation of Raman spectra of disordered and amorphous carbon. *Phys. Rev. B* **2000**, *61*, 14095–14107. [[CrossRef](#)]
76. Ferrari, A.C. Raman spectroscopy of graphene and graphite: Disorder, electron-phonon coupling, doping and nonadiabatic effects. *Solid State Commun.* **2007**, *143*, 47–57. [[CrossRef](#)]
77. Woehrl, N.; Ochedowski, O.; Gottlieb, S.; Shibasaki, K.; Schulz, S. Plasma-enhanced chemical vapor deposition of graphene on copper substrates. *AIP Adv.* **2014**, *4*, 047128. [[CrossRef](#)]
78. Muhl, S.; Méndez, J.M. A Review of the preparation of carbon nitride film. *Diam. Relat. Mater.* **1999**, *8*, 1809–1830. [[CrossRef](#)]
79. Chakradhar, A.; Sivapragasam, N.; Nayakasinghe, M.T.; Burghaus, U. Support effects in the adsorption of water on CVD graphene: An ultra-high vacuum adsorption study. *Chem. Commun.* **2015**, *51*, 11463–11466. [[CrossRef](#)] [[PubMed](#)]
80. Chen, Y.; Yang, X.-C.; Liu, Y.-J.; Zhao, J.-X.; Cai, Q.-H.; Wang, X.-Z. Can Si-doped graphene activate or dissociate O<sub>2</sub> molecule? *J. Mol. Gr. Model.* **2013**, *39*, 126–132. [[CrossRef](#)] [[PubMed](#)]
81. Ellingham, H.J.T. Reproducibility of oxides and sulphides in metallurgical processes. *J. Soc. Chem. Ind.* **1944**, *63*, 125–133.
82. Luo, Z.; Yu, T.; Shang, J.; Wang, Y.; Lim, S.; Liu, L.; Gurzadyan, G.G.; Shen, Z.; Lin, J. Large-scale synthesis of bi-layer graphene in strongly coupled stacking order. *Adv. Funct. Mater.* **2011**, *21*, 911–917. [[CrossRef](#)]
83. Kuper, C.A.; Labes, M.M. A new method of doping pyrolytic graphite utilizing laser heating in the presence of organic heteroatomic vapors. *Chem. Mater.* **1999**, *11*, 408–411. [[CrossRef](#)]
84. Marton, D.; Boyd, K.J.; Al-Bayati, A.H.; Todorov, S.S.; Rabalais, J.W. Carbon nitride deposited using energetic species: A two-phase system. *Phys. Rev. Lett.* **1994**, *73*, 118–121. [[CrossRef](#)]
85. Dresselhaus, S.; Dresselhaus, G.; Avouris, P. *Carbon Nanotubes: Synthesis, Structure, Properties, and Applications*, 1st ed.; Springer: Berlin/Heidelberg, Germany, 2001; pp. 1–448. [[CrossRef](#)]
86. Ripalda, J.M.; Montero, I.; Galán, L. An XPS study of carbon nitride synthesized by ion beam nitridation of C<sub>60</sub> fullerene. *Diam. Relat. Mater.* **1998**, *7*, 402–406. [[CrossRef](#)]
87. Hellgren, N.; Johansson, M.P.; Broitman, E.; Hultman, L.; Sundgren, J.-E. Role of nitrogen in the formation of hard and elastic CN<sub>x</sub> thin films by reactive magnetron sputtering. *Phys. Rev. B* **1999**, *59*, 5162–5169. [[CrossRef](#)]
88. Ronning, C.; Feldermann, H.; Merk, R.; Hofsäsa, H.; Reinke, P.; Thiele, J.-U. Carbon nitride deposited using energetic species: A review on XPS studies. *Phys. Rev. B* **1998**, *58*, 2207–2215. [[CrossRef](#)]
89. Liu, A.Y.; Cohen, M.L. Prediction of new low compressibility solids. *Science* **1989**, *245*, 841–842. [[CrossRef](#)] [[PubMed](#)]
90. Wu, P.; Du, P.; Zhang, H.; Cai, C. Microscopic effects of the bonding configuration of nitrogen-doped graphene on its reactivity toward hydrogen peroxide reduction reaction. *Phys. Chem. Chem. Phys.* **2013**, *15*, 6920–6928. [[CrossRef](#)]
91. Sjöström, H.; Stafström, S.; Boman, M.; Sundgren, J.-E. Superhard and Elastic Carbon Nitride Thin Films Having Fullerenelike Microstructure. *Phys. Rev. Lett.* **1995**, *75*, 1336–1339. [[CrossRef](#)]
92. Shamir, N.; Baldwin, D.A.; Darko, T.; Rabalais, J.W.; Hochmann, P. Reactions of homonuclear diatomic ions with metal surfaces. II. Nitridation of Al, Cu, Mo, and Ni by N<sup>2+</sup> beams in the low kinetic energy-near threshold region. *J. Chem. Phys.* **1982**, *76*, 6417–6424. [[CrossRef](#)]
93. Li, X.; Magnuson, C.W.; Venugopal, A.; An, J.; Suk, J.W.; Han, B.; Borysiak, M.; Cai, W.; Velamakanni, A.; Zhu, Y.; et al. Graphene films with large domain size by a two-step chemical vapor deposition process. *Nano Lett.* **2010**, *10*, 4328–4334. [[CrossRef](#)]
94. Wofford, J.M.; Nie, S.; McCarty, K.F.; Bartelt, N.C.; Dubon, O.D. Graphene islands on Cu foils: The interplay between shape, orientation, and defects. *Nano Lett.* **2010**, *10*, 4890–4896. [[CrossRef](#)] [[PubMed](#)]
95. Zhao, J.; Shaygan, M.; Eckert, J.; Meyyappan, M.; Rummeli, M.H. A growth mechanism for free-standing vertical graphene. *Nano Lett.* **2014**, *14*, 3064–3071. [[CrossRef](#)] [[PubMed](#)]

96. Zhao, X.; Outlaw, R.A.; Wang, J.J.; Zhu, M.Y.; Smith, G.D.; Holloway, B.C. Thermal desorption of hydrogen from carbon nanosheets. *J. Chem. Phys.* **2006**, *124*, 194704. [[CrossRef](#)] [[PubMed](#)]
97. Wood, J.D.; Schmucker, S.W.; Lyons, A.S.; Pop, E.; Lyding, J.W. Effects of polycrystalline Cu substrate on graphene growth by chemical vapor deposition. *Nano Lett.* **2011**, *11*, 4547–4554. [[CrossRef](#)] [[PubMed](#)]
98. Hao, Y.; Bharathi, M.S.; Wang, L.; Liu, Y.; Chen, H.; Nie, S.; Wang, X.; Chou, H.; Tan, C.; Fallahazad, B.; et al. The Role of surface oxygen in the growth of large single-crystal graphene on copper. *Science* **2013**, *342*, 720–723. [[CrossRef](#)] [[PubMed](#)]



© 2019 by the authors. Licensee MDPI, Basel, Switzerland. This article is an open access article distributed under the terms and conditions of the Creative Commons Attribution (CC BY) license (<http://creativecommons.org/licenses/by/4.0/>).